CMS Physics Analysis Summary

Measurement of the inclusive and differential $t\bar{t}\gamma$ cross section and EFT interpretation in the dilepton channel at $\sqrt{s} = 13\,\text{TeV}$

The CMS Collaboration

Abstract

The production cross section of a top quark pair in association with a photon is measured in pp collisions in the decay channel with two oppositely charged leptons ($e^{\pm}\mu^{\mp}$, $e^{+}e^{-}$, $\mu^{+}\mu^{-}$). The data set of $138\,\text{fb}^{-1}$ was recorded by the CMS experiment at $\sqrt{s} = 13\,\text{TeV}$ during the 2016 to 2018 data-taking period of the CERN LHC. A fiducial phase space is defined such that photons radiated by initial-state particles, top quarks, or any of their decay products are included. An inclusive cross section of $174.4 \pm 2.5\,(\text{stat}) \pm 6.1\,(\text{syst})\,\text{fb}$ is measured in a signal region with at least one b-tagged jet and exactly one photon with transverse momentum above $20\,\text{GeV}$. Differential cross sections are measured as a function of several kinematic observables of the photon, leptons, and jet, and compared to standard model predictions. The measurements are also interpreted in the standard model effective field theory framework, and limits on the relevant Wilson coefficients are combined with a previous CMS measurement of the same production process using single-lepton events.

1   Introduction

The cross section measurement of top quark pair production in association with a photon ($t\bar{t}\gamma$) probes the electroweak top quark-photon coupling ($t\gamma$), both making it a test of the standard model (SM) of particle physics and providing sensitivity for potential modifications from new physics beyond the SM. With the large amount of data collected with the CMS detector in proton-proton (pp) collisions at $\sqrt{s} = 13\,\text{TeV}$ during the data-taking period from 2016 to 2018 of the CERN LHC, precise measurements are possible even of relatively small cross sections such as for $t\bar{t}\gamma$ production. We present inclusive and differential measurements of the $t\bar{t}\gamma$ production cross section in final states with two oppositely charged leptons ($e^{\pm}\mu^{\mp}$, $e^{+}e^{-}$, or $\mu^{+}\mu^{-}$). The inclusion of differential information improves the strength of the constraints that can be set from the measurement. Additionally, we perform a model-independent interpretation of the results in terms of the SM effective field theory (SMEFT).

First evidence for $t\bar{t}\gamma$ production was found by the CDF Collaboration in $p\bar{p}$ collisions at $\sqrt{s} = 1.96\,\text{TeV}$ [1]. At the LHC, $t\bar{t}\gamma$ production in pp collisions was first observed by the ATLAS Collaboration at $\sqrt{s} = 7\,\text{TeV}$ [2]. Further measurements were performed by the ATLAS and CMS Collaborations at $\sqrt{s} = 8\,\text{TeV}$ [3, 4] and 13 TeV [5–7]. The latest measurement by the CMS Collaboration uses the same data set as this analysis in a complementary event selection with one lepton (electron or muon) in the final state [7].

For this measurement, a fiducial phase space is defined for the $t\bar{t}\gamma$ signal process with criteria on the kinematic properties of the photon, leptons, jets at the particle level. Events are included where the photon is radiated by an incoming quark, a top quark, or any of the charged decay products of the top quark. Examples of leading-order (LO) Feynman diagrams for these processes are shown in Fig. 1.
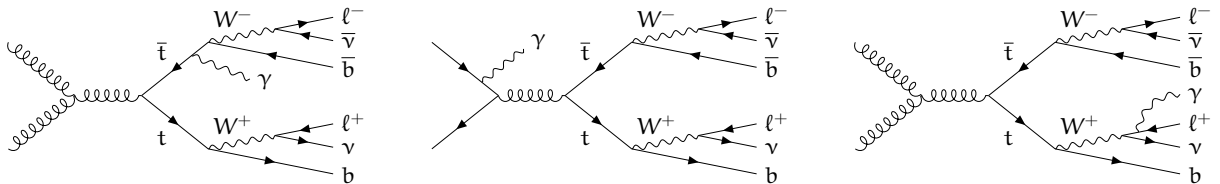

Figure 1: Leading-order Feynman diagrams for $t\bar{t}\gamma$ production with two leptons in the final state, where the photon is radiated by a top quark (left), by an incoming quark (middle), and by one of the charged decay products of a top quark (right).

Events are selected with two oppositely charged leptons, an isolated photon, and at least one jet. Background contributions without top quarks are reduced by applying additional b tagging criteria on the selected jet. After the event selection, the dominant source of background stems from events with nonprompt photons, i.e. photons originating from particles inside hadronic jets or from additional pp collisions, or hadronic jets misidentified as photons. The nonprompt background contribution is estimated with a data-driven method, while other background sources are estimated from Monte Carlo (MC) event simulations. The inclusive cross section is measured with a profile likelihood method from the measured distribution of the transverse momentum p_{T} of the reconstructed photon. The differential cross sections are measured by subtracting the estimated background contributions from the measured distributions and applying an unfolding method to correct for detector resolution effects. To evaluate the sensitivity to possible modifications of the $t\gamma$ coupling, the measured photon p_{T} distribution is used to constrain the c_{tZ} and c_{tZ}^{I} Wilson coefficients in the SMEFT framework, as defined in Ref. [8].

The SM production of $t\bar{t}\gamma$ has been studied at next-to-leading-order (NLO) precision in quantum chromodynamics (QCD) and electroweak theory [9–14], also including the top quark de-

cays and photons radiated off the final-state particles at full NLO accuracy [15, 16]. The sensitivity to new-physics modifications has been studied for anomalous dipole moments of the top quark [17–19] and in the SMEFT context [20–22]. The possibility to study charge asymmetries in $t\bar{t}\gamma$ production has been investigated in Refs. [23, 24].

This note is organized as follows. In Section 2, the data and MC samples used in this measurement are discussed. The reconstruction and selection of events is detailed in Section 3, followed by the estimation of the background contributions in Section 4. Systematic uncertainties that affect the measurements are discussed in Section 5. The results of the inclusive and the differential cross section measurements are presented in Sections 6 and 7, respectively. In Section 8, the interpretation of the measurements in the SMEFT framework is provided. All results are summarized in Section 9.

2 Data and simulated samples

The data sample used in this measurement corresponds to an integrated luminosity of $138\,\text{fb}^{-1}$ of pp collision events at $\sqrt{s} = 13\,\text{TeV}$ collected with the CMS detector between 2016 and 2018. To account for the differences in the LHC running conditions and the CMS detector performance, the data collected in the three years of data taking are analyzed separately and appropriate per-year calibrations are applied, before the data are combined for the final cross section measurements.

Simulated MC events are used for the evaluation of the signal selection efficiency, the validation of the data-driven background estimates, and the prediction of other background contributions. Three separate sets of simulated event samples are used, corresponding to the conditions of the three years of data taking.

For the $t\bar{t}\gamma$ signal process, simulated events are generated at LO accuracy in QCD using the MADGRAPH5_aMC@NLO event generator [25]. The $t\bar{t}\gamma$ sample is normalized to the cross section evaluated with MADGRAPH5_aMC@NLO at NLO accuracy. For the simulation of background events from $t\bar{t}$, $t\bar{t}H$, and single top t-channel and tW production, the POWHEG v2 event generator [26–31] at NLO accuracy in QCD is used. Samples for $gg \to ZZ$ production are generated at LO accuracy in QCD with the MCFM event generator [32, 33]. For all other background processes, events are simulated with the MADGRAPH5_aMC@NLO event generator at LO or NLO accuracy in QCD. In the simulation of the hard process, the NNPDF3.0 (NNPDF3.1) [34, 35] parton distribution functions (PDFs) are used for the 2016 (2017 and 2018) samples. All event generators are interfaced with the PYTHIA8 simulation [36, 37] for parton showering and hadronization. The underlying event is modelled using the CP5 tune [38], except for some 2016 samples for which the CUETP8M1, CUETP8M2, and CUETP8M2T4 tunes [39–41] are used. For the samples generated with MADGRAPH5_aMC@NLO at LO (NLO) accuracy and interfaced with PYTHIA8, matrix element calculations are merged with the parton showering using the MLM (FxFx) [42, 43] matching scheme. A summary of all simulated samples is given in Table 1.

An overlap exists between the phase space modelled in the $t\bar{t}\gamma$ and $t\bar{t}$ samples because of the addition of soft photons to simulated events by the PYTHIA8 simulation. To ensure orthogonal phase spaces, simulated events from the $t\bar{t}\gamma$ sample are only used if they contain a generated photon with $p_T > 10\,\text{GeV}$ and $|\eta| < 5$ that does not originate from the decay of a meson and is separated from any other generated stable particle (except neutrinos and photons) by $\Delta R = \sqrt{\Delta\eta^2 + \Delta\varphi^2} > 0.1$, where $\Delta\eta$ and $\Delta\varphi$ are the differences in pseudorapidity and azimuthal angle, respectively, between the directions of the photon and the stable particle.

Table 1: MC event generators used to simulate events for the signal and background processes. For each simulated process, the order of the cross section normalization calculation, the MC event generator used, and the perturbative order in QCD of the generator calculation are shown. The order is given as LO, NLO, next-to-next-to-leading order (NNLO), and including next-to-next-to-leading-logarithmic (NNLL) corrections. The symbol V refers to W and Z bosons.

Process	Cross section normalization	Event generator	Perturbative order in QCD
$t\bar{t}\gamma$	NLO	MADGRAPH5_aMC@NLO	LO
Z+jets	NNLO [44]	MADGRAPH5_aMC@NLO	LO
$Z\gamma, W\gamma, VV, VVV, t\bar{t}Z, t\bar{t}W, tZq, tWZ, tHq, tHW, t\bar{t}VV, t\bar{t}t\bar{t}$	NLO	MADGRAPH5_aMC@NLO	NLO
$t\bar{t}$	NNLO+NNLL [45]	POWHEG	NLO
single t (t channel)	NLO [46, 47]	POWHEG	NLO
single t (s channel)	NLO [46, 47]	MADGRAPH5_aMC@NLO	NLO
tW	NNLO [48]	POWHEG	NLO
$t\bar{t}H$	NLO	POWHEG	NLO
$gg \rightarrow ZZ$	LO	MCFM	LO

Conversely, simulated events from the $t\bar{t}$ sample are only used if they do not contain such a photon. Similarly, the overlap between the $Z\gamma$ and Z+jets sample is removed, with modified requirements of $p_T > 15\,$GeV and $|\eta| < 2.6$ for the generated photon and a minimum distance of $\Delta R > 0.05$.

The $t\bar{t}\gamma$ cross section is measured in a fiducial phase space defined at particle level after the event generation, parton showering, and hadronization of the $t\bar{t}\gamma$ event sample. Electrons and muons, after adding all photons inside a cone of $\Delta R < 0.1$ around the lepton direction, are required to have $p_T > 15\,$GeV and $|\eta| < 2.4$. Photons must have $p_T > 20\,$GeV and $|\eta| < 1.4442$, and be isolated from any other stable particle except for neutrinos by more than $\Delta R > 0.1$. Additionally, photons must be separated from electrons and muons by more than $\Delta R > 0.4$. Jets are clustered with the anti-k_T algorithm [49] with a distance parameter $R = 0.4$ using all particles excluding neutrinos, are required to have $p_T > 30\,$GeV and $|\eta| < 2.4$, and must be isolated from leptons and photons by $\Delta R > 0.4$ and 0.1, respectively. The flavour of the jets is determined with a ghost-matching method [50], and those jets matched to b hadrons are tagged as b jets. The fiducial phase space is defined by requiring $t\bar{t}\gamma$ events to have exactly one photon, at least one b jet, and exactly two oppositely charged leptons with an invariant mass $m(\ell\ell) > 20\,$GeV, of which at least one has $p_T > 25\,$GeV. The fiducial phase space definition requirements are summarized in Table 2. The SM prediction for the $t\bar{t}\gamma$ cross section in this fiducial phase space is $\sigma_{SM}(pp \rightarrow t\bar{t}\gamma) = 153 \pm 25\,$fb, evaluated at NLO accuracy, where the uncertainty includes scale variations and the PDF choice.

For all simulated events, the CMS detector response is subsequently modelled with the GEANT4 framework [51]. Additional minimum-bias pp interactions in the same or nearby bunch crossing, referred to as pileup, are added from simulation as well. All events in the data and simulated samples are reconstructed with the same algorithms described in Section 3. Corrections for differences in the selection performance between data and simulated samples are applied to simulated events.

Table 2: Summary of the fiducial region definition for the various objects at particle level. The "isolated" definition for the photon requires no stable particle (except neutrinos) with $p_T >$ 5 GeV within a cone of $\Delta R = 0.1$. The parameters N_ℓ, N_γ, and N_b represent the number of leptons, photons, and b jets, respectively, in the event.

Leptons	Photons	Jets	b jets	Events
$p_T > 25(15)$ GeV	$p_T > 20$ GeV	$p_T > 30$ GeV	$p_T > 30$ GeV	$N_\ell = 2$
$|\eta| < 2.4$	$|\eta| < 1.4442$	$|\eta| < 2.4$	$|\eta| < 2.4$	$N_\gamma = 1$
	$\Delta R(\gamma, \ell) > 0.4$	$\Delta R(\text{jet}, \ell) > 0.4$	$\Delta R(\text{jet}, \ell) > 0.4$	$N_b \geq 1$
	isolated	$\Delta R(\text{jet}, \gamma) > 0.1$	$\Delta R(\text{jet}, \gamma) > 0.1$	$m(\ell\ell) > 20$ GeV
			matched to b hadron	

3 Event reconstruction and selection

Information from the various subdetectors is used by the particle-flow algorithm [52] to reconstruct the particles (photons, electrons, muons, charged and neutral hadrons) produced in an event. The candidate vertex with the largest value of summed physics-object p_T^2 is taken to be the primary pp interaction vertex (PV). The physics objects are jets, clustered using the jet finding algorithm [49, 53] with the tracks assigned to candidate vertices as inputs, and the associated missing transverse momentum, taken as the negative vector sum of the p_T of those jets.

The signature of an electron consists of a charged particle track matched with one or more energy deposits in the electromagnetic calorimeter (ECAL), produced by the electron and any bremsstrahlung photons emitted collinearly with its trajectory throughout the tracker. The energy of the electron is calculated based on the curvature of the track and the ECAL energy deposits of the electron and any photons it radiated [54]. Muons are associated with the presence of energy deposits in the gas-ionization chambers compatible with a charged path in the inner tracker [55]. Electron and muon candidates with $p_T > 15$ GeV and $|\eta| < 2.4$ that pass the identification requirements described in Ref. [56] are selected. The identification requirements are optimized to discriminate between "prompt" leptons originating from decays of heavy vector bosons and top quarks, and "nonprompt" leptons that originate from hadron decays, or are jets or hadrons misidentified as leptons. To that end, discriminating variables are combined into a boosted decision tree discriminant trained with the TMVA toolkit [57]. The discriminating variables are the kinematic properties of the lepton and the jet closest to the lepton; relative isolation variables defined as scalar p_T sums of all particles within cones around the lepton direction, divided by the lepton p_T; properties of the impact parameter of the associated tracks of the leptons, computed with respect to the PV position; the muon segment compatibility [55] in the case of muons; and the discriminator value of a standard electron identification algorithm [54] in the case of electrons. Additionally, electrons with $1.4442 < |\eta| < 1.566$ in the gap between the ECAL barrel and endcaps are removed.

Photons are identified based on the presence of an energy deposit in the ECAL with no charged particle tracks pointing towards this deposit. The photon energy is obtained using this ECAL measurement, to which corrections for the energy scale and zero suppression are applied in both simulation and data. In simulated events, smearing corrections are applied to photons to match the resolution observed in data [54]. Photon candidates are considered with $p_T > 20$ GeV and $|\eta| < 1.4442$, i.e. inside the barrel region of the detector. Identification criteria are imposed on photon candidates based on the shower shape, the isolation of the photon, and hits in the pixel tracker compatible with the photon direction, which improves the rejection of elec-

trons, misidentified hadrons, and photons produced within jets. One shower shape criterion is a requirement on $\sigma_{\eta\eta}$, a measure of the electromagnetic shower width in units of the ECAL crystal spacing, to fulfil $\sigma_{\eta\eta} < 0.01015$, thus rejecting hadronic jets, which typically produce a wider shower. One of the isolation criteria is a requirement on the charged isolation of $I_{\text{chg}} < 1.141\,\text{GeV}$, where I_{chg} is computed as the scalar p_{T} sum of all charged hadrons compatible with the PV and inside a cone of $\Delta R < 0.3$ around the photon direction [54]. For a veto on additional reconstructed photons, the two criteria $\sigma_{\eta\eta} < 0.01015$ and $I_{\text{chg}} < 1.141\,\text{GeV}$ are not imposed. Additionally, photons must be isolated from selected leptons by requiring that $\Delta R(\gamma, \ell) < 0.4$.

Jets are clustered using all particle-flow candidates with the anti-k_{T} algorithm [49] and a distance parameter of $R = 0.4$. To mitigate the impact of pileup on the jet momentum, tracks identified to be originating from pileup vertices are discarded and an offset correction is applied to correct for remaining contributions. Jet energy corrections are derived from simulation studies so that the average measured energy of jets becomes identical to that of particle-level jets. In situ measurements of the momentum balance in dijet, photon+jet, Z+jet, and multijet events are used to determine any residual differences between the jet energy scale in data and simulation, and appropriate corrections are made [58]. Additional selection criteria are applied to each jet to remove jets potentially dominated by instrumental effects or reconstruction failures. Reconstructed jets with $p_{\text{T}} > 30\,\text{GeV}$ and $|\eta| < 2.4$ are selected if they are separated from any selected lepton by $\Delta R > 0.4$, and any selected photon by $\Delta R > 0.1$. Jets originating from the hadronization of b quarks are identified (b tagged) with the DeepCSV heavy-flavour jet tagging algorithm [59], using a working point with an efficiency of about 70% and a misidentification rate of 12% (1%) for jets originating from c quarks (light quarks or gluons).

A combination of trigger paths requiring the presence of one or two leptons is used to select events. The p_{T} threshold with the single-lepton trigger paths was 27 GeV and 24 GeV in 2016, and 32 GeV and 27 GeV in 2017 and 2018 for electrons and muons, respectively. For the double-lepton trigger paths, the p_{T} thresholds were 23 GeV and 17 GeV for the highest-p_{T} (leading) and 12 GeV and 8 GeV for the second-highest-p_{T} (subleading) electron and muon, respectively. The trigger efficiency for events passing the lepton selection described below is higher than 95%, as measured from events selected with an independent trigger.

Events are selected with exactly two leptons with opposite charges, exactly one photon, and at least one b-tagged jet. The two leptons are required to have an invariant mass $m(\ell\ell) > 20\,\text{GeV}$ to reduce background contributions with nonprompt leptons and from light QCD resonances. The requirement of a b jet reduces background contributions from processes without top quarks. To further reduce the background from $Z\gamma$ production, events where the two leptons or the two leptons and the photon have an invariant mass close to the Z boson mass, $|m(\ell\ell) - m_Z| < 15\,\text{GeV}$ or $|m(\ell\ell\gamma) - m_Z| < 15\,\text{GeV}$, are removed, where m_Z is the world-average Z boson mass [60].

The observed yields in data, together with the signal yields expected from the MC event samples, and the predicted background yields as described in Section 4, before applying the fit described in Section 6, are shown in Figs. 2 and 3 for a selection of observables.

4 Background estimation

Contributions to the final state with two leptons, one photon, and at least one b-tagged jet arise from several SM processes. A distinction is made between events with a prompt or a nonprompt photon. For simulated events of all considered processes, the reconstructed photon
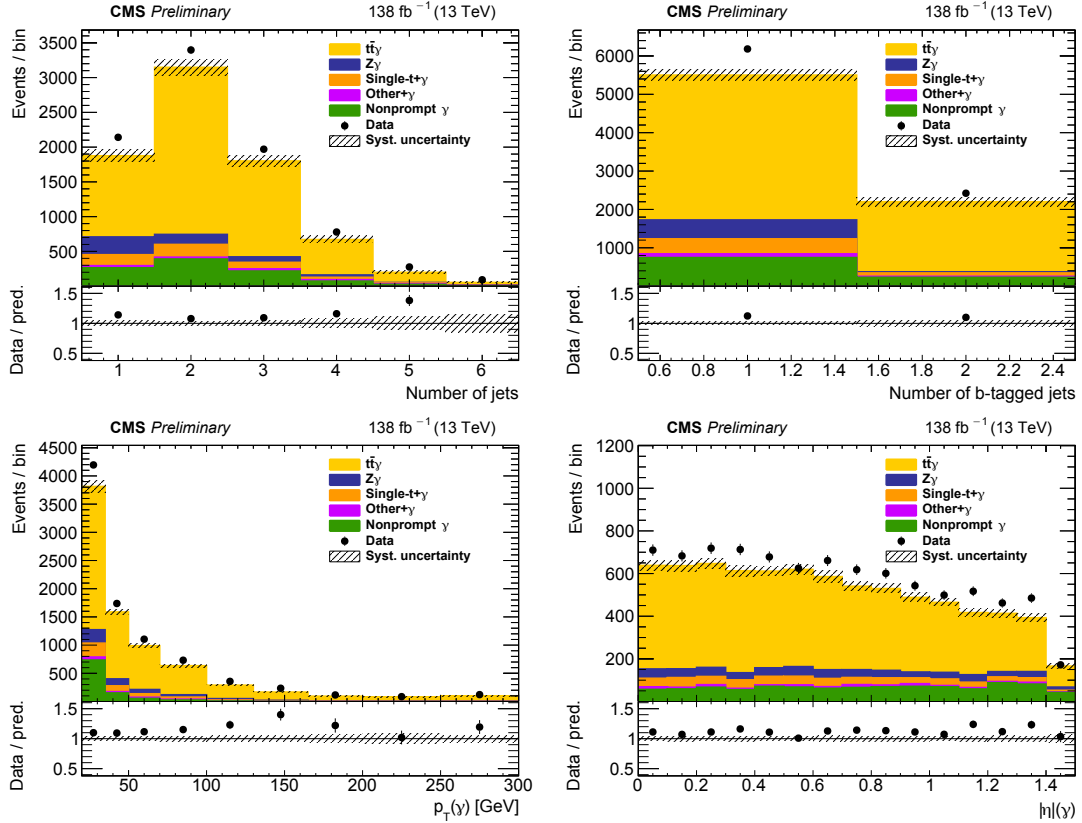
Figure 2: The observed (points) and the predicted (shaded histograms) signal and background yields as a function of the number of jets (upper left) and b-tagged jets (upper right), and of the p_T (lower left) and $|\eta|$ (lower right) of the photon, after applying the signal selection. Distributions are shown with all relevant corrections applied, but without scaling of the signal in accordance with the inclusive fit results. The vertical bars on the points show the statistical uncertainties in the data, and the band the systematic uncertainty in the predictions. The lower panels show the ratio of the event yields in data to the overall sum of the predictions.

is classified as "prompt" if it is matched to a generated photon that originates from a lepton, quark, or boson. If the match is a photon originating from other types of particles (typical for photons radiated from charged mesons), if there is only a match to other types of particles (typical for electrons misidentified as photons), or if no match is found (typical for photons from pileup interactions), it is classified as "nonprompt".

Background contributions with prompt photons are estimated from the simulated event samples. The most important contributions arise from $Z\gamma$ production and single top quark processes (*t* channel, *s* channel, and tW) in association with a photon. These two categories are treated separately, while all other processes with prompt photons are grouped as "other+γ". Based on the precision of cross section measurement results of the major background contributions [61–63], normalization uncertainties of 5%, 10%, and 30% are assigned to the $Z\gamma$, tγ, and other+γ background predictions, respectively. To improve the modelling of the $Z\gamma$ prediction with high jet multiplicities, correction factors are derived in data samples orthogonal to the signal selection, as detailed in Section 4.1. For all background contributions with nonprompt photons, a data-driven estimation is used as described in Section 4.2.
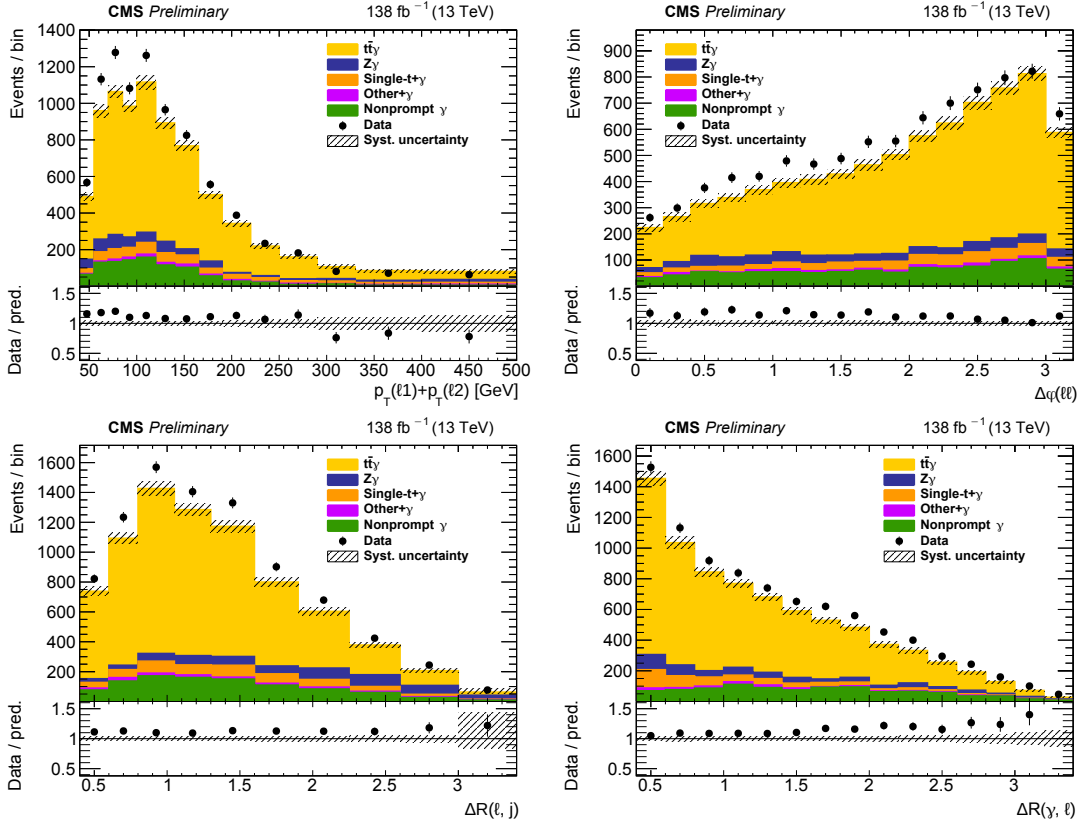
Figure 3: The observed (points) and the predicted (shaded histograms) signal and background yields as a function of the scalar p_T sum (upper left) and the ϕ difference (upper right) of the two leptons, and of the ΔR between the photon and the closest jet (lower left) or the closest lepton (lower right), after applying the signal selection. Distributions are shown with all relevant corrections applied, but without scaling of the signal in accordance with the inclusive fit results. The vertical bars on the points show the statistical uncertainties in the data, and the band the systematic uncertainty in the predictions. The lower panels show the ratio of the event yields in data to the overall sum of the predictions.

4.1 The Zγ control region

Prompt photons in Zγ production events originate either from initial-state radiation (ISR) from an incoming quark or final-state radiation (FSR) from one of the leptons in the Z boson decay. To validate the simulation of the Zγ prediction, a control region in data is defined with an inverted $m(\ell\ell\gamma)$ requirement for events with a same-flavour lepton pair (e$^+$e$^-$ or $\mu^+\mu^-$), which enriches the selection of events where the reconstructed photon originates from FSR in Z+jets production. By keeping the $m(\ell\ell)$ requirement unchanged, the contribution from Z+jets production events with nonprompt photons remains small.

In Fig. 4, the measured and predicted yields are compared as a function of the reconstructed photon p_T and of the number of jets, N_j, and b-tagged jets, N_b. The shape of the photon p_T is well described, but a clear mismodelling is observed in the distributions of jet and b jet multiplicity. We derive correction factors as a function of N_j and N_b, which are applied in the signal selection to the Zγ background yields. No correction factors are applied to e$^\pm\mu^\mp$ events since the Zγ yield is negligible.

The data yields are found in bins of (N_j, N_b), and the statistical uncertainty in each bin yield is included in the data-driven correction factor uncertainties. Additionally, the normalization
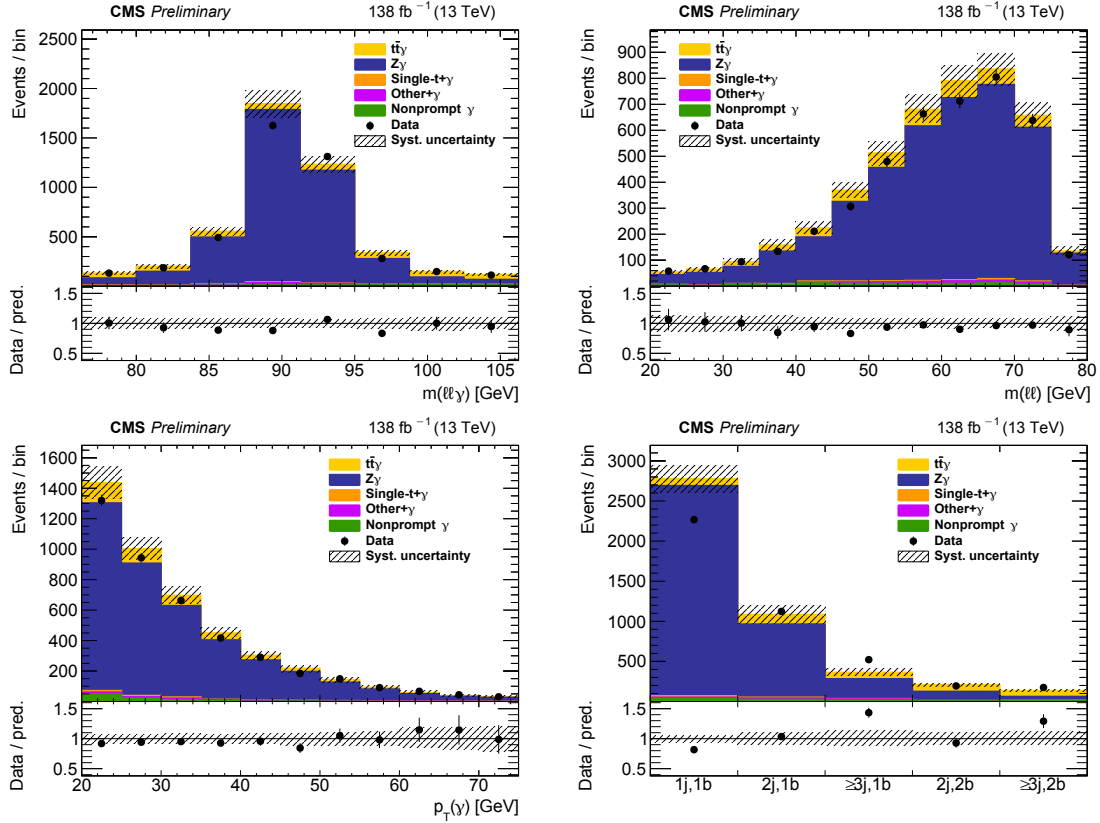
Figure 4: The observed (points) and predicted (shaded histograms) event yields as a function of $m(\ell\ell\gamma)$ (upper left), $m(\ell\ell)$ (upper right), photon p_T (lower left), and the number of jets and b-tagged jets (lower right), after applying the event selection for the $Z\gamma$ control region. The vertical lines on the points show the statistical uncertainties in the data, and the band the total uncertainty in the predictions. The lower panels show the ratio of the event yields in data to the predictions.

of the signal contamination in the $Z\gamma$ control region is considered as a source of systematic uncertainty. With a cross section normalization uncertainty of 18.5% and a fraction of $t\bar{t}\gamma$ events in the control region of 9.7%, the resulting normalization uncertainty in the $Z\gamma$ yield in the signal region is 1.8%.

The correction factors significantly improve the precision of the prediction for FSR photons in Z+jets production events. After signal selection, FSR photons contribute about 70% to the total yield of $Z\gamma$ background events. The contribution of ISR photons to the $Z\gamma$ background is not constrained by using the control region, and thus retains a normalization uncertainty of 5% [62], resulting in an additional uncertainty of 1.5% in the normalization of the total $Z\gamma$ yield.

4.2 Nonprompt photon background

The contribution of background processes with nonprompt photons is estimated with a data-driven "tight-to-loose ratio" method. A transfer factor f is defined as the ratio of the number of nonprompt photon events where the photon passes the identification criteria to the number where it fails. It is used to predict the number of nonprompt photon events in the signal region, N_{SR}, from the observed number of events in a sideband region enriched with nonprompt photon events, N_{SB}, as $N_{SR} = f N_{SB}$.

The sideband region contains events that pass the signal selection except for having a photon that fails the $\sigma_{\eta\eta}$ identification criterion. To increase the fraction of nonprompt photon events to more than 95%, the photon is required to have $\sigma_{\eta\eta} > 0.012$. For the evaluation of f, a measurement region with nonisolated photon events is defined by inverting the charged isolation requirement on the reconstructed photon to $1.141 < I_{chg} < 15\,\mathrm{GeV}$. To increase the amount of data in the measurement region for events with same-flavour leptons, the $N_b \geq 1$ requirement is replaced by the looser requirement of $N_j \geq 1$ for $e^{\pm}\mu^{\mp}$ events. The sideband of the measurement region has a fraction of nonprompt photon events of larger than 99.5%. The transfer factor is measured separately in bins of p_T and $|\eta|$ of the reconstructed photon. Contributions from prompt photon events in the measurement region and both sideband regions are estimated from simulated event samples and subtracted before the evaluation of N_{SR}.
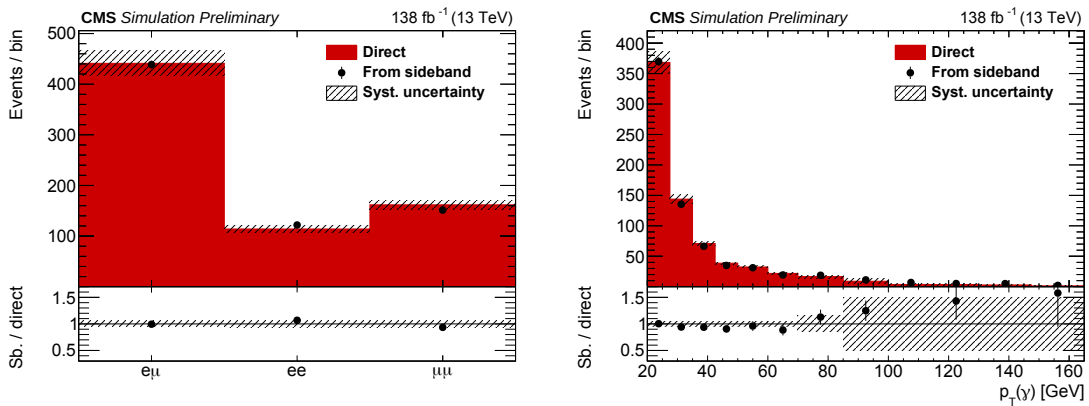

Figure 5: Event yields in the signal region predicted from a simulated $t\bar{t}$ event sample (shaded histogram) and estimated from applying the transfer factor to the event yields of the same sample in the sideband region (points), as a function of the lepton flavour (left) and the photon p_T (right). The vertical lines on the points show the statistical uncertainties from the simulated event samples, and the band the total systematic uncertainty assigned to the nonprompt photon background estimate. The lower panels show the ratio between the two predictions.

We validate the performance of the nonprompt photon background estimate with simulated event samples. The transfer factors are measured from $t\bar{t}$ and Z+jets samples since the measurement region is enriched in these two processes. In the signal selection, however, the contribution from Z+jets production is minimal, and thus the nonprompt photon background contribution in the signal selection is estimated from $t\bar{t}$ samples in the sideband region alone, and compared to the direct prediction of the $t\bar{t}$ samples for the signal region. The comparison is shown in Fig. 5, and shows good agreement between the two predictions at the level of 5%, which is assigned as a flat systematic uncertainty. Only at large reconstructed photon p_T does the use of the transfer factor result in an overprediction of the nonprompt photon background contribution. Hence, we assign an additional uncertainty of 50% to the predicted event yields where the reconstructed photon has $p_T > 80\,\mathrm{GeV}$.

5   Systematic uncertainties

Systematic uncertainties affect the signal selection efficiency, the predicted and measured background yields, and the measured distributions. For each source of systematic uncertainty, variations of the predicted signal and background yields are evaluated in the relevant distributions, and either used to construct nuisance parameters in the fits employed for the inclusive cross section measurement and the EFT interpretation, or to repeat the differential cross section

Table 3: Summary of the sources of statistical and systematic uncertainties in the $t\bar{t}\gamma$ cross section measurements. The first column lists the source of the uncertainty. The second column indicates the treatment of correlations between the uncertainties in the three years of data taking, where ✓ means fully correlated, $\sim$ means partially correlated, and $\times$ means uncorrelated. For each systematic source, the uncertainty before applying the fit is estimated from a cut-and-count analysis of the predicted and observed event yields separately in bins of $p_{\mathrm{T}}(\gamma)$ and for the three years of data taking using the input variations; the typical range across the three years is shown in the third column and can be compared between the different uncertainty sources. The last column gives the impact of each uncertainty on the measured inclusive $t\bar{t}\gamma$ cross section after the fit to the data, the so-called postfit uncertainties.

	Source	Correlation	Uncertainty [%] Prefit range	Postfit
Experimental	Integrated luminosity	$\sim$	1.3–3.2	1.7
	Pileup	✓	0.1–1.4	0.6
	Trigger efficiency	$\times$	0.6–1.7	0.6
	Electron selection efficiency	$\sim$	1.0–1.3	1.1
	Muon selection efficiency	$\sim$	0.3–0.5	0.5
	Photon selection efficiency	$\sim$	0.4–3.7	0.9
	Jet energy scale	$\sim$	0.1–1.3	0.5
	Jet energy resolution	✓	0.0–0.6	<0.1
	b tagging efficiency	$\sim$	0.9–1.4	1.1
	L1 prefiring	✓	0.0–0.8	0.3
Theoretical	Choice in μ_{F} and μ_{R}	✓	0.3–3.5	1.5
	PDF choice	✓	0.3–4.5	0.2
	PS modelling: ISR & FSR scale	✓	0.3–3.5	1.2
	PS modelling: colour reconnection	✓	0.0–8.4	0.2
	PS modelling: b fragmentation	✓	0.0–2.2	0.6
	Underlying event tune	✓	0.5	0.5
Background	$Z\gamma$ correction & normalization	✓	0.0–0.2	<0.1
	$t\gamma$ normalization	✓	0.0–0.9	0.8
	Other+γ normalization	✓	0.3–1.0	0.8
	Nonprompt γ normalization	✓	0.0–1.8	0.9
	Size of simulated samples	$\times$	1.5–7.6	0.9
	Total systematic uncertainty			3.6
	Statistical uncertainty			1.4
	Total uncertainty			3.9

measurement and evaluate the uncertainty in the unfolded distribution. A summary of all systematic uncertainties and the estimated impact on the measured inclusive cross section is given in Table 3. Additionally, the table indicates the treatment of the uncertainties between the 2016, 2017, and 2018 data sets as uncorrelated, partially correlated, or fully correlated.

The integrated luminosities of the 2016, 2017, and 2018 data-taking periods are individually

known with uncertainties of 1.2, 2.3, and 2.5%, respectively [64–66]. Some systematic effects in the calibration of the luminosity measurements are correlated, such that the uncertainty in the integrated luminosity of the combined data set is 1.6%. The uncertainty in the integrated luminosity affects both the normalization of the background contributions predicted from data, as well as the extraction of the measured cross section from the final estimate of the number of signal events. Thus, the impact can be larger than the input uncertainty, and also depends on the fraction of nonprompt photon background events not affected by the luminosity uncertainty.

Simulated events are reweighted such that the simulated distribution of the number of interactions in each bunch crossing matches the expected distribution, assuming a total inelastic pp cross section of 69.2 mb [67]. The uncertainty in this cross section of 4.6% [68] is used to produce varied signal and background predictions, fully correlated between the three years of data taking.

The efficiency of the trigger selection is corrected in simulated events to match the efficiency in data measured from two separate classes of independent trigger paths based on hadronic activity or missing transverse momentum signatures. The scale factors depend on the momentum of the two selected leptons and deviate from unity by up to 20% for low-p_T electrons. The statistical uncertainty in the trigger efficiency measurement is treated as uncorrelated between the three years of data taking, while the difference between the trigger efficiencies measured from the two classes of independent trigger paths is assigned as a correlated systematic uncertainty.

For the reconstruction, identification, and isolation of electrons, muons, and photons, the efficiencies are measured with a "tag-and-probe" method [54, 55] separately in data and simulated events. Scale factors are applied to simulated events to correct for differences, and uncertainties are evaluated by varying the scale factors, separately for electrons, muons, and photons. Statistical (systematic) sources of uncertainties in the efficiency measurements are treated as uncorrelated (correlated) between the three years of data taking.

Uncertainties in the jet energy calibration and resolution corrections are evaluated by varying the transverse momenta of the reconstructed jets in simulated events separately for the several uncertainty sources described in Ref. [58]. For each source, two separate variations that are either fully correlated or uncorrelated between the three years of data taking are considered.

Differences in the b tagging efficiency between data and simulated events are corrected by applying scale factors to simulated events. Uncertainties are evaluated by varying the scale factors separately for light- and heavy-flavour jets, where both correlated and uncorrelated variations between the three years of data taking are considered [59].

During the 2016 and 2017 data-taking periods, the ECAL level-1 (L1) trigger in the forward endcap region ($|\eta| > 2.4$) exhibited a gradual shift in the timing of its inputs, leading to a specific inefficiency known as "prefiring". The effect was found to be most relevant in events with jets reconstructed with $2.4 < |\eta| < 3.0$ and $p_T > 100$ GeV, affecting also measurements that do not directly select on such jets. A correction determined from an unbiased data sample is applied, and 20% of the correction is assigned as the associated uncertainty.

Several theoretical uncertainties in the event simulation are considered. To evaluate the impact in the choice of the factorization scale μ_F and the renormalization scale μ_R, these two parameters are scaled up and down by a factor of 2, individually and simultaneously, and the envelope of the variations is taken to estimate the uncertainty. The choice of the PDF set is evaluated by using the replicas in the NNPDF PDFs [34, 35] and taking the root-mean-square of the variations as an estimate of the uncertainty. The choice of μ_F for ISR and FSR in the parton shower simulation is separately varied up and down by a factor of 2. The default colour reconnection

model in the parton shower simulation is replaced by three alternative models [69, 70], and only a small impact on the results is found. The uncertainty in the b fragmentation function is evaluated by varying the parameters of the Bowler–Lund function [71]. Finally, the uncertainty in the underlying event tune [38, 41] results in a 0.5% variation of the predicted signal yield. All theoretical uncertainties are treated as correlated between the three years of data taking.

For all background predictions, normalization uncertainties as detailed in Section 4 are included in the measurements, and treated as correlated between the three years of data taking. For the background predictions using simulated event samples, the statistical uncertainty in the MC prediction is included as a systematic uncertainty as well.

6   Inclusive cross section measurement

The inclusive cross section is extracted following the statistical procedure described in Refs. [72, 73] from a profile likelihood fit to the reconstructed photon p_T distribution. The binned likelihood function $L(r, \theta)$ is constructed as the product of the Poisson probabilities to obtain the observed yields given the predicted signal and background estimates in each event category, and includes terms to account for the systematic uncertainties and their correlation pattern as described in Section 5 as well. The event categories are the bins of the photon p_T distribution separately for each year of data taking and for the three lepton flavour channels. The signal strength modifier r scales the normalization of the predicted signal estimate, and θ denotes a full set of nuisance parameters representing the systematic uncertainties including the normalization of the background predictions.

The quantities $\hat{r}$ and $\hat{\theta}$ denote the signal strength and nuisance parameter set that simultaneously maximize the likelihood function. Similarly, $\hat{\theta}_r$ maximizes the likelihood function for a fixed value of r. From the test statistics $q(r) = -2 \ln L(r, \hat{\theta}_r)/L(\hat{r}, \hat{\theta})$, based on the profile likelihood function, the observed cross section is extracted with an asymptotic approximation [72, 73]. The distribution of the reconstructed photon p_T per lepton flavour channel after performing the fit is shown in Fig. 6, combined for the three years of data taking. The fiducial cross section for $t\bar{t}\gamma$ production in the dilepton final state is measured to be

$$\sigma_{\text{fid}}(\text{pp} \to t\bar{t}\gamma) = 174.4 \pm 2.5 \,(\text{stat}) \pm 6.1 \,(\text{syst}) \,\text{fb}. \tag{1}$$

The predicted cross section of $\sigma_{\text{SM}}(\text{pp} \to t\bar{t}\gamma) = 153 \pm 25 \,\text{fb}$ is smaller than the measurement, but in agreement considering the large uncertainty in the prediction. Consistent results are found when fitting the flavour channels separately, as shown in Fig. 7. The impact of the different systematic uncertainty sources on the inclusive cross section measurements are summarized in Table 3. No strong constraints on the background yields and systematic uncertainty sources were found. The leading contributions to the systematic uncertainty arise from the uncertainty in the integrated luminosity, the choice in μ_F and μ_R in the signal simulation, the PS modelling, and the b tagging and electron selection efficiencies.

The simulated $t\bar{t}\gamma$ samples used in the cross section measurement were generated assuming a top quark mass of 172.5 GeV. The impact of the experimental 0.4 GeV uncertainty in the top quark mass [60] on the acceptance is evaluated by reweighting the simulated events to match the Breit–Wigner shapes of the accordingly varied top quark mass, resulting in a change of 0.5% in the measured cross section.
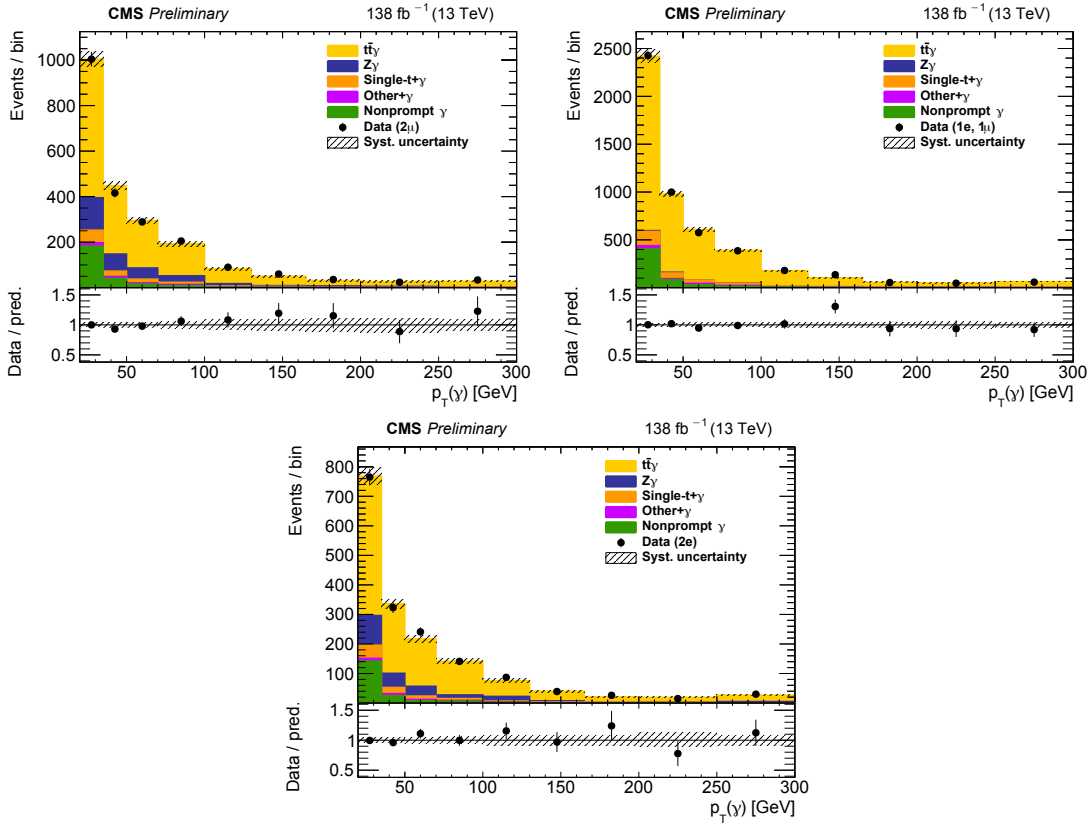
Figure 6: The observed (points) and predicted (shaded histograms) event yields as a function of the reconstructed photon p_T after applying the signal selection, for the $\mu^+\mu^-$ (upper left), $e^\pm\mu^\mp$ (upper right), and e^+e^- (lower) channels, after the values of the normalizations and nuisance parameters obtained in the fit are applied. The vertical bars on the points show the statistical uncertainties in the data, and the band the systematic uncertainty in the predictions. The lower panels of each plot show the ratio of the event yields in data to the predictions.
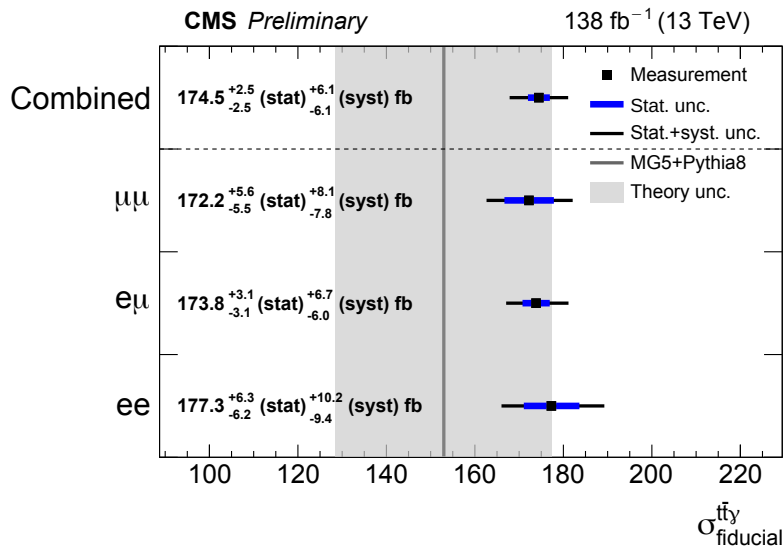

Figure 7: Fiducial $t\bar{t}\gamma$ production cross section in the dilepton final state measured for different lepton flavour channels, and the combined result, compared to the SM prediction at NLO accuracy. The shaded band shows the uncertainty in the prediction.

7 Differential cross section measurement

The differential cross section in the fiducial phase space is measured as a function of twelve observables defined in Table 4. For each observable, variable bin sizes are chosen to optimize the statistical uncertainty in the measured event yields and limit the number of bin-to-bin migrations. In each bin of the reconstructed distributions, the yield is determined by subtracting the predicted background yields as well as the expected yield of $t\bar{t}\gamma$ events outside of the fiducial phase space from the measured event yields.

Table 4: Definition of the observables used in the differential cross section measurement.

Symbol	Definition
$p_T(\gamma)$	transverse momentum of the photon
$|\eta|(\gamma)$	absolute value of the pseudorapidity of the photon
$\Delta R(\gamma, \ell)$	angular separation between the photon and the closest lepton
$\Delta R(\gamma, \ell_1)$	angular separation between the photon and the leading lepton
$\Delta R(\gamma, \ell_2)$	angular separation between the photon and the subleading lepton
$\Delta R(\gamma, b)$	angular separation between the photon and the closest b jet
$\Delta R(\ell, j)$	smallest angular separation between any of the selected leptons and jets
$|\Delta\eta(\ell\ell)|$	pseudorapidity difference between the two leptons
$\Delta\varphi(\ell\ell)$	azimuthal angle difference between the two leptons
$p_T(\ell\ell)$	transverse momentum of the dilepton system
$p_T(\ell_1) + p_T(\ell_2)$	scalar sum of the transverse momenta of the two leptons
$p_T(j_1)$	transverse momentum of the leading jet

Both detector response and acceptance effects are represented by response matrices derived from the $t\bar{t}\gamma$ MADGRAPH5_aMC@NLO simulated event samples, choosing half the number of bins of the reconstructed distribution for the fiducial phase space observable, and including the same corrections and scale factors as used in the inclusive cross section measurement. The differential cross section is then evaluated by applying an unfolding procedure. The resolutions of the considered observables are found to be good, with a very small number of events migrating from one bin to another. Under such conditions, matrix inversion without regularization is an unbiased and stable method to correct for detector response and acceptance [74]. We apply the TUnfold package [75] to evaluate the differential cross section from the background-subtracted measured event yields and the response matrices.

All systematic uncertainties described in Section 5 are applied in the differential cross section measurement. The theoretical uncertainties are evaluated by repeating the unfolding procedure with varied response matrices. For the experimental uncertainties, the relative variation of the total signal and background predictions are evaluated, and this variation is then applied to the data before the subtraction of the varied background predictions. The background normalization uncertainties are evaluated by varying the background subtraction.

The resulting differential cross sections are shown in Figs. 8 and 9 as absolute and in Figs. 10 and 11 as normalized distributions. The measurements are compared to two cross section predictions obtained at particle level, generated with the MADGRAPH5_aMC@NLO event generator interfaced with parton shower simulations provided by PYTHIA8 with the CP5 tune and by HERWIG7 [76] v7.1.4 with the CH3 tune [77]. The prediction using PYTHIA8 is shown with its uncertainty from scale variations and the PDF choice. The agreement between the measured distribution and the prediction using PYTHIA8 is evaluated by calculating a χ^2 value including
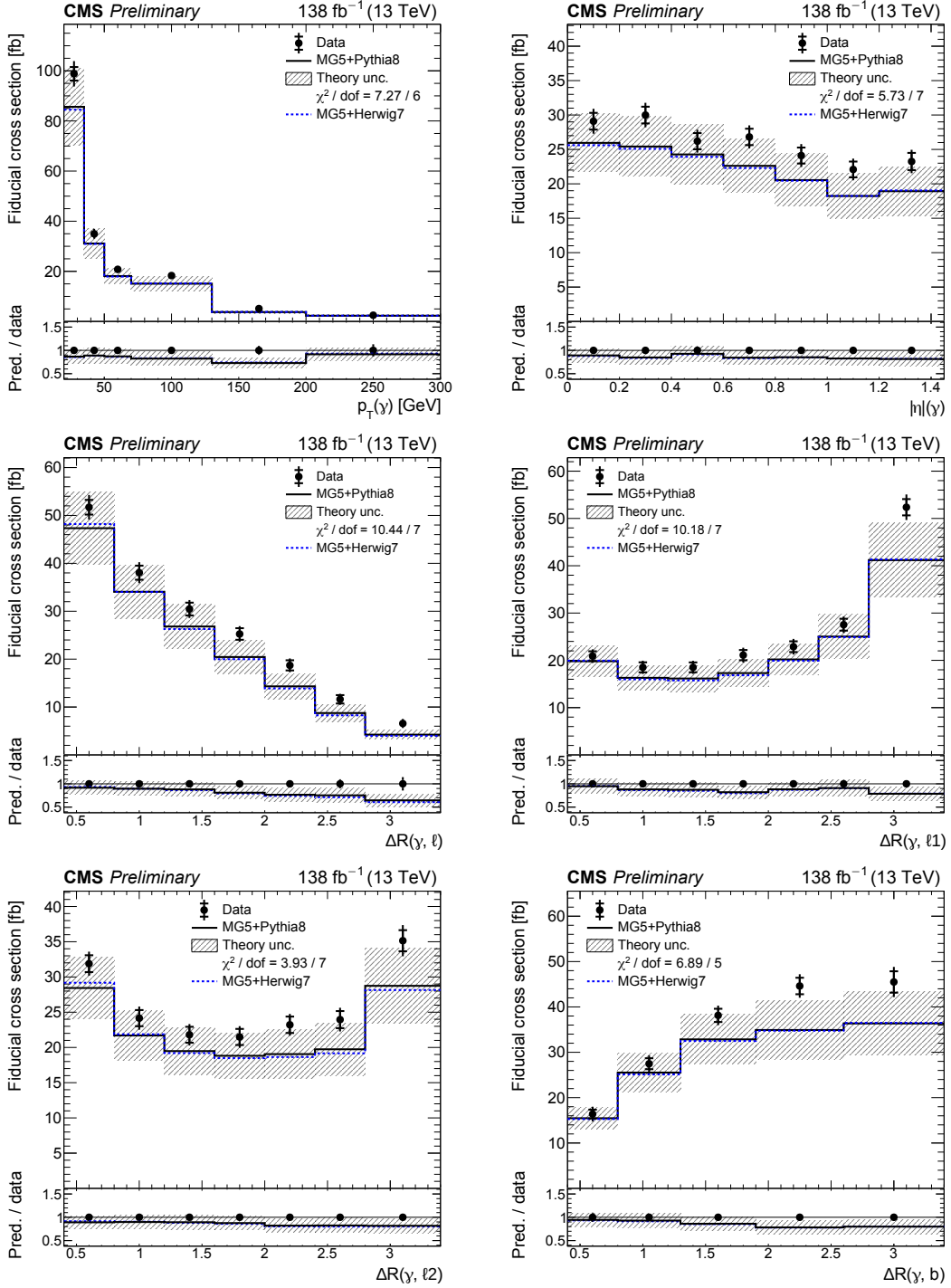
Figure 8: Absolute differential $t\bar{t}\gamma$ production cross sections as a function of $p_T(\gamma)$ (upper left), $|\eta|(\gamma)$ (upper right), $\Delta R(\gamma, \ell)$ (middle left), $\Delta R(\gamma, \ell_1)$ (middle right), $\Delta R(\gamma, \ell_2)$ (lower left), and $\Delta R(\gamma, b)$ (lower right), as defined in Table 4. The data are represented by points, with inner (outer) vertical bars indicating the statistical (total) uncertainties. The predictions obtained with the MADGRAPH5_aMC@NLO event generator interfaced with different parton shower simulations, as described in the text, are shown as horizontal lines. The theoretical uncertainties in the prediction using PYTHIA8 are indicated by shaded bands. The lower panels display the ratios of the predictions to the measurement. The values of the χ^2 divided by the number of degrees of freedom (dof) quantifying the agreement between the measurement and the PYTHIA8 prediction are indicated in the legends.
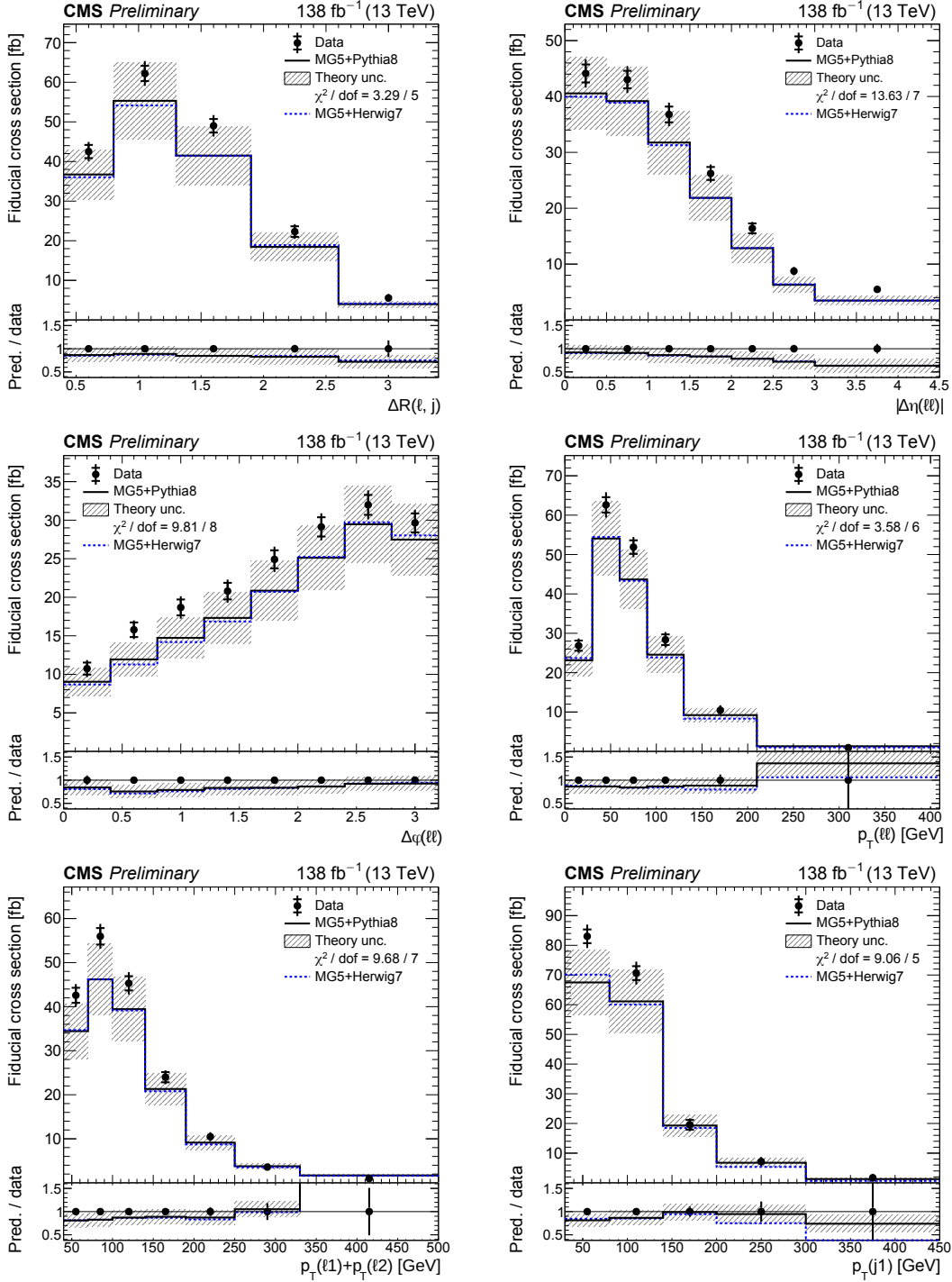
Figure 9: Absolute differential $t\bar{t}\gamma$ production cross sections as a function of $\Delta R(\ell, j)$ (upper left), $|\Delta\eta(\ell\ell)|$ (upper right), $\Delta\varphi(\ell\ell)$ (middle left), $p_T(\ell\ell)$ (middle right), $p_T(\ell_1) + p_T(\ell_2)$ (lower left), and $p_T(j_1)$ (lower right), as defined in Table 4. The data are represented by points, with inner (outer) vertical bars indicating the statistical (total) uncertainties. The predictions obtained with the MADGRAPH5_aMC@NLO event generator interfaced with different parton shower simulations, as described in the text, are shown as horizontal lines. The theoretical uncertainties in the prediction using PYTHIA8 are indicated by shaded bands. The lower panels display the ratios of the predictions to the measurement. The values of the χ^2 divided by the number of degrees of freedom (dof) quantifying the agreement between the measurement and the PYTHIA8 prediction are indicated in the legends.
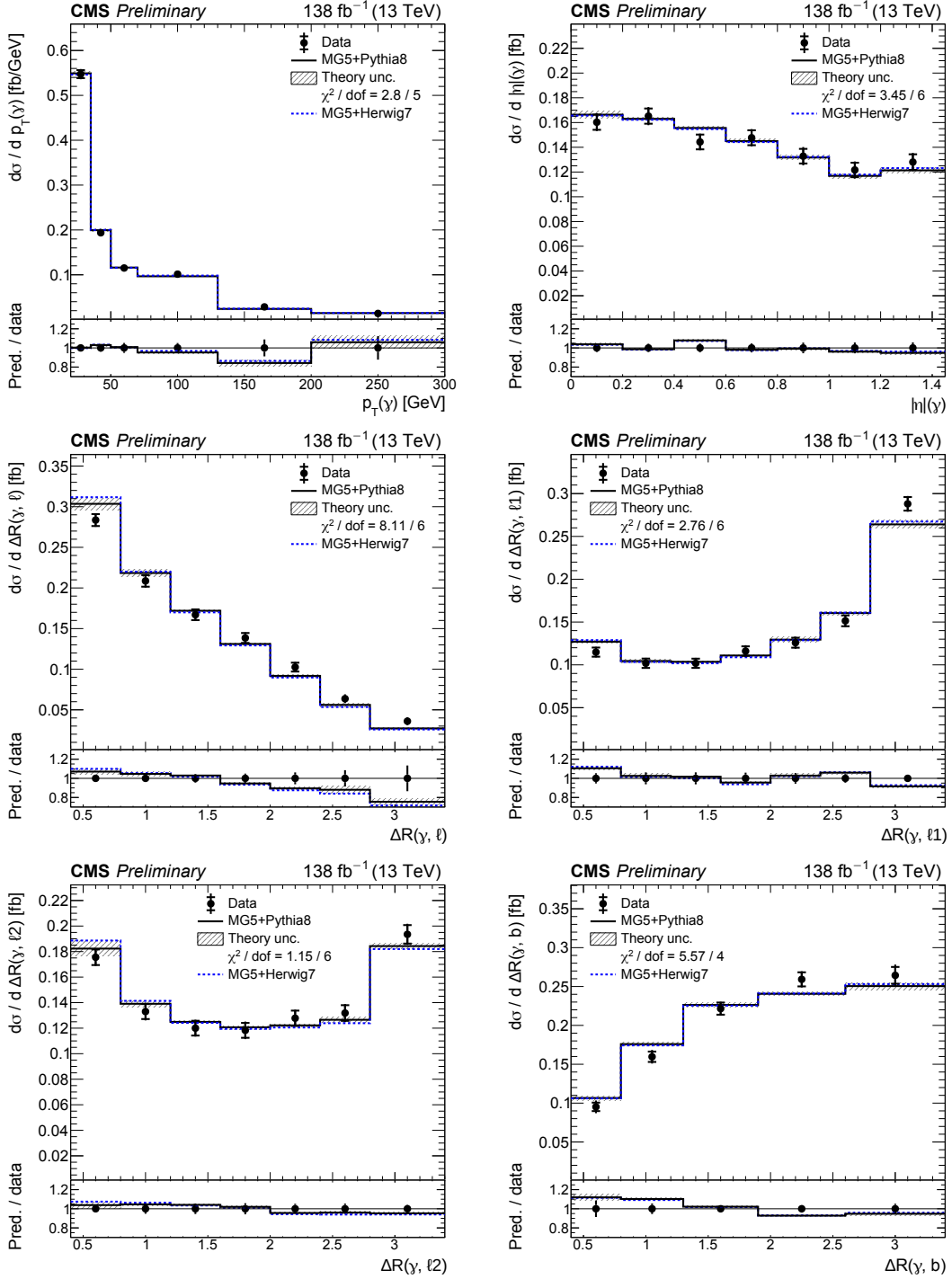
Figure 10: Normalized differential $t\bar{t}\gamma$ production cross sections as a function of $p_T(\gamma)$ (upper left), $|\eta|(\gamma)$ (upper right), $\Delta R(\gamma, \ell)$ (middle left), $\Delta R(\gamma, \ell_1)$ (middle right), $\Delta R(\gamma, \ell_2)$ lower left), and $\Delta R(\gamma, b)$ (lower right), as defined in Table 4. The data are represented by points, with inner (outer) vertical bars indicating the statistical (total) uncertainties. The predictions obtained with the MADGRAPH5_AMC@NLO event generator interfaced with different parton shower simulations, as described in the text, are shown as horizontal lines. The theoretical uncertainties in the prediction using PYTHIA8 are indicated by shaded bands. The lower panels display the ratios of the predictions to the measurement. The values of the χ^2 divided by the number of degrees of freedom (dof) quantifying the agreement between the measurement and the PYTHIA8 prediction are indicated in the legends.
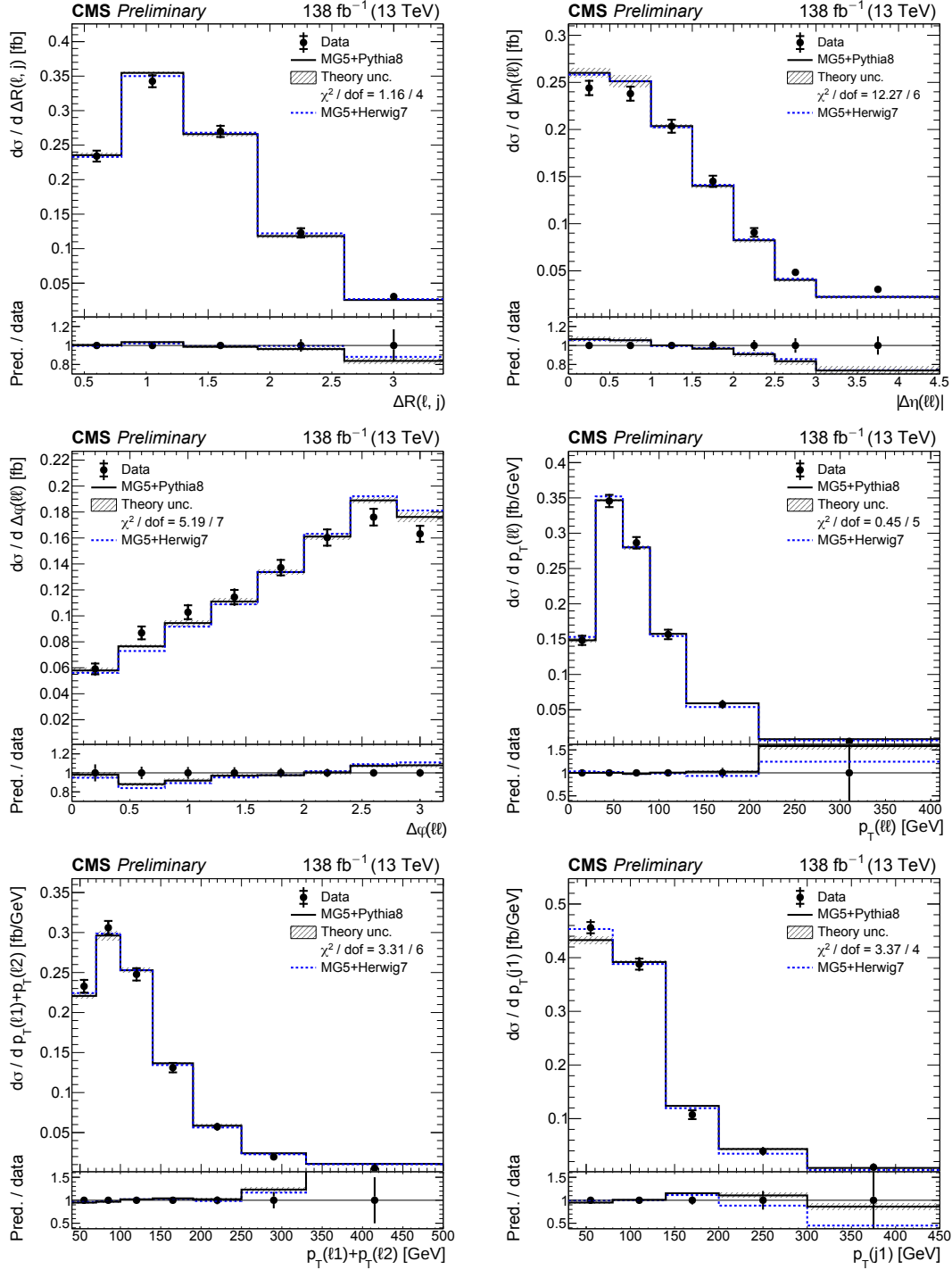
Figure 11: Normalized differential $t\bar{t}\gamma$ production cross sections as a function of $\Delta R(\ell, j)$ (upper left), $|\Delta\eta(\ell\ell)|$ (upper right), $\Delta\varphi(\ell\ell)$ (middle left), $p_T(\ell\ell)$ (middle right), $p_T(\ell_1) + p_T(\ell_2)$ (lower left), and $p_T(j_1)$ (lower right), as defined in Table 4. The data are represented by points, with inner (outer) vertical bars indicating the statistical (total) uncertainties. The predictions obtained with the MADGRAPH5_aMC@NLO event generator interfaced with different parton shower simulations, as described in the text, are shown as horizontal lines. The theoretical uncertainties in the prediction using PYTHIA8 are indicated by shaded bands. The lower panels display the ratios of the predictions to the measurement. The values of the χ^2 divided by the number of degrees of freedom (dof) quantifying the agreement between the measurement and the PYTHIA8 prediction are indicated in the legends.

the full uncertainties in both the measurement and the prediction, which is indicated on the figures.

8   Effective field theory interpretation

To constrain potential new-physics effects in the $t\bar{t}\gamma$ production process, an interpretation is performed in the SMEFT framework using the Warsaw basis [20, 21]. Of the 59 baryon-number-conserving dimension-six Wilson coefficients, 15 are found to be relevant for top quark interactions [78, 79]. While anomalous interactions between the top quark and the gluon are strongly constrained by measurements of $t\bar{t}$ production [80, 81], the measurement of $t\bar{t}\gamma$ production provides sensitivity to the electroweak dipole moments of the top quark, denoted by $C_{uB}^{(33)}$ and $C_{uW}^{(33)}$ [8], because of the SM gauge symmetries complementary to the sensitivity provided by $t\bar{t}Z$ production [17–19]. The coefficients describing the modifications of the $t\bar{t}Z$ interaction vertex, c_{tZ} and c_{tZ}^{I}, and of the $t\bar{t}\gamma$ interaction vertex, $c_{t\gamma}$ and $c_{t\gamma}^{I}$, are expressed in the Warsaw basis as linear combinations of $C_{uB}^{(33)}$ and $C_{uW}^{(33)}$:

$$c_{tZ} = \text{Re}\left(-\sin\theta_W C_{uB}^{(33)} + \cos\theta_W C_{uW}^{(33)}\right),$$
$$c_{tZ}^{I} = \text{Im}\left(-\sin\theta_W C_{uB}^{(33)} + \cos\theta_W C_{uW}^{(33)}\right),$$
$$c_{t\gamma} = \text{Re}\left(\cos\theta_W C_{uB}^{(33)} - \sin\theta_W C_{uW}^{(33)}\right),$$
$$c_{t\gamma}^{I} = \text{Im}\left(\cos\theta_W C_{uB}^{(33)} - \sin\theta_W C_{uW}^{(33)}\right).$$

The modification of the Wtb vertex is already tightly constrained by measurements of W helicity fractions [82]. Under the assumption of an SM Wtb vertex with $C_{uW}^{(33)} = 0$, the $t\bar{t}Z$ and $t\bar{t}\gamma$ modifications are dependent, and we choose to parameterize the new-physics hypothesis in terms of c_{tZ} and c_{tZ}^{I}.

The effect of these modifications is probed in the measured distribution of the photon p_T at the reconstructed level, which is also used in the inclusive cross section measurement. The other observables studied in the differential cross section measurement are found to be largely insensitive to these new-physics effects. Keeping all other Wilson coefficients at their SM values and setting the SMEFT expansion parameter to a mass scale of $\Lambda = 1\,\text{TeV}$, the expected SMEFT modifications for nonzero values of c_{tZ} and c_{tZ}^{I} are estimated at particle level and used to calculate per-event weights corresponding to the ratio of the predicted SM and SMEFT cross sections in bins of photon p_T. The nominal simulation is then reweighted after applying the full analysis selection criteria to the reconstructed events to estimate the expected SMEFT modifications at detector level. This procedure follows closely the strategy described in Ref. [7].

The constraints on the Wilson coefficients are measured from a profile likelihood fit constructed in the same way as for the inclusive cross section measurement. The set of nuisance parameters is extended by the uncertainty in the $t\bar{t}\gamma$ signal normalization. The minimized likelihood value obtained in a fit using the SMEFT-predicted photon p_T distribution is compared to the corresponding likelihood value using the SM prediction. One-dimensional scans of the negative log-likelihood value difference to the best-fit value are shown in Fig. 12 for each Wilson coefficient, where the other Wilson coefficient is set to zero in the fit. The corresponding intervals at 68 and 95% confidence level (CL) are listed in Table 5. Furthermore, a fit is performed where both Wilson coefficients are varied simultaneously in the fit. The result of the two-dimensional

scan in shown in Fig. 13. The SM prediction is within the 68% CL of the best-fit values of the c_{tZ} and c_{tZ}^{I} coefficients.
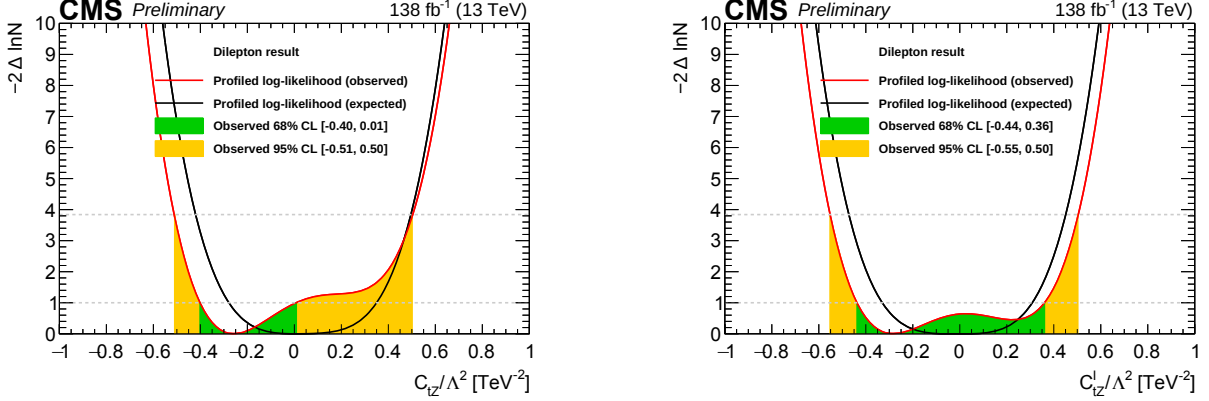

Figure 12: Expected (black) and observed (red) results from the one-dimensional scans of the Wilson coefficients c_{tZ} (left) and c_{tZ}^{I} (right) from the interpretation of this result. In the scans, the other Wilson coefficient is set to zero. The green (yellow) bands indicate the 68% (95%) CL contours of the Wilson coefficients.

Table 5: Summary of the one-dimensional CL intervals obtained for the Wilson coefficients c_{tZ} and c_{tZ}^{I} from the interpretation of this result. The profiled results correspond to the fits where the other Wilson coefficient is left free in the fit, otherwise it is set to zero.

	Wilson coefficient		68% CL interval $(\Lambda/\text{TeV})^2$	95% CL interval $(\Lambda/\text{TeV})^2$
Expected	c_{tZ}	$c_{tZ}^{I} = 0$	$[-0.28, 0.36]$	$[-0.42, 0.50]$
		profiled	$[-0.36, 0.44]$	$[-0.49, 0.56]$
	c_{tZ}^{I}	$c_{tZ} = 0$	$[-0.33, 0.31]$	$[-0.48, 0.46]$
		profiled	$[-0.42, 0.40]$	$[-0.54, 0.51]$
Observed	c_{tZ}	$c_{tZ}^{I} = 0$	$[-0.41, 0.01]$	$[-0.51, 0.51]$
		profiled	$[-0.47, 0.42]$	$[-0.57, 0.58]$
	c_{tZ}^{I}	$c_{tZ} = 0$	$[-0.44, 0.37]$	$[-0.55, 0.51]$
		profiled	$[-0.49, 0.43]$	$[-0.60, 0.55]$

The similar measurement by CMS using final states with one lepton presented in Ref. [7] probes an orthogonal fiducial phase space of the $t\bar{t}\gamma$ production process. To further improve the constraints on the Wilson coefficients, a combined EFT interpretation of both measurements is performed. While the measurement presented here is very pure in $t\bar{t}\gamma$ production events and is limited by systematic uncertainty sources, the measurement in Ref. [7] has a significantly larger number of signal events at large values of photon p_T, providing good sensitivity to modifications described by the studied Wilson coefficients. As a result, the two measurements complement each other well in the combined interpretation. To that end, a combined profile likelihood function is constructed, based on the photon p_T distributions measured in dilepton and single-lepton events. The evaluation is performed as described for the dilepton-only interpretation above. The one-dimensional scans of the Wilson coefficients separately are shown in Fig. 14, and the corresponding 68 and 95% CL intervals are listed in Table 6. The result of the two-dimensional scan is shown in Fig. 15. The obtained constraints improve the results of
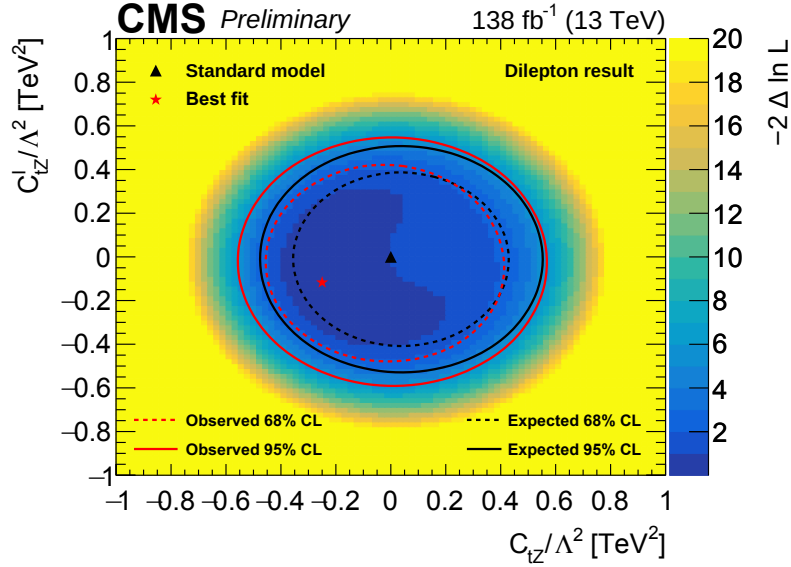
Figure 13: Observed result from the two-dimensional scan of the Wilson coefficients c_{tZ} and c_{tZ}^{I} from the interpretation of this result. The shading quantified by the colour scale on the right reflects the negative log-likelihood ratio with respect to the best fit value that is indicated by the star. The 68% (dashed) and 95% (solid) CL contours are shown with red (black) lines for the observed (expected) result. The triangle indicates the SM prediction.
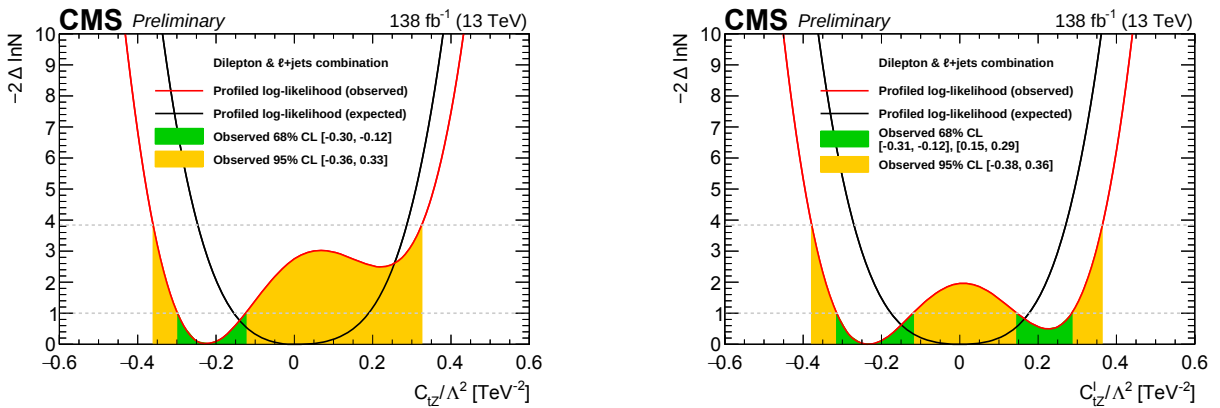
Figure 14: Expected (black) and observed (red) results from the one-dimensional scans of the Wilson coefficients c_{tZ} (left) and c_{tZ}^{I} (right) from the combined interpretation of this result and the lepton+jets result from Ref. [7]. In the scans, the other Wilson coefficient is set to zero. The green (yellow) bands indicate the 68% (95%) CL contours of the Wilson coefficients.

Table 6: Summary of the one-dimensional CL intervals obtained for the Wilson coefficients c_{tZ} and c_{tZ}^{I} from the combined interpretation of this result and the lepton+jets result from Ref. [7]. The profiled results correspond to the fits where the other Wilson coefficient is left free in the fit, otherwise it is set to zero.

			68% CL interval $(\Lambda/\text{TeV})^2$	95% CL interval $(\Lambda/\text{TeV})^2$
Expected	c_{tZ}	$c_{tZ}^{I} = 0$	$[-0.16, 0.19]$	$[-0.25, 0.29]$
		profiled	$[-0.22, 0.26]$	$[-0.29, 0.33]$
	c_{tZ}^{I}	$c_{tZ} = 0$	$[-0.18, 0.18]$	$[-0.27, 0.27]$
		profiled	$[-0.24, 0.24]$	$[-0.32, 0.32]$
Observed	c_{tZ}	$c_{tZ}^{I} = 0$	$[-0.30, -0.12]$	$[-0.37, 0.33]$
		profiled	$[-0.34, 0.23]$	$[-0.40, 0.38]$
	c_{tZ}^{I}	$c_{tZ} = 0$	$[-0.32, -0.11], [0.15, 0.29]$	$[-0.38, 0.37]$
		profiled	$[-0.33, 0.31]$	$[-0.40, 0.39]$

Figure 15: Observed result from the two-dimensional scan of the Wilson coefficients c_{tZ} and c_{tZ}^{I} from the combined interpretation of this result and the lepton+jets result from Ref. [7]. The shading quantified by the colour scale on the right reflects the negative log-likelihood ratio with respect to the best fit value that is indicated by the star. The 68% (dashed) and 95% (solid) CL contours are shown with red (black) lines for the observed (expected) result. The triangle indicates the SM prediction.
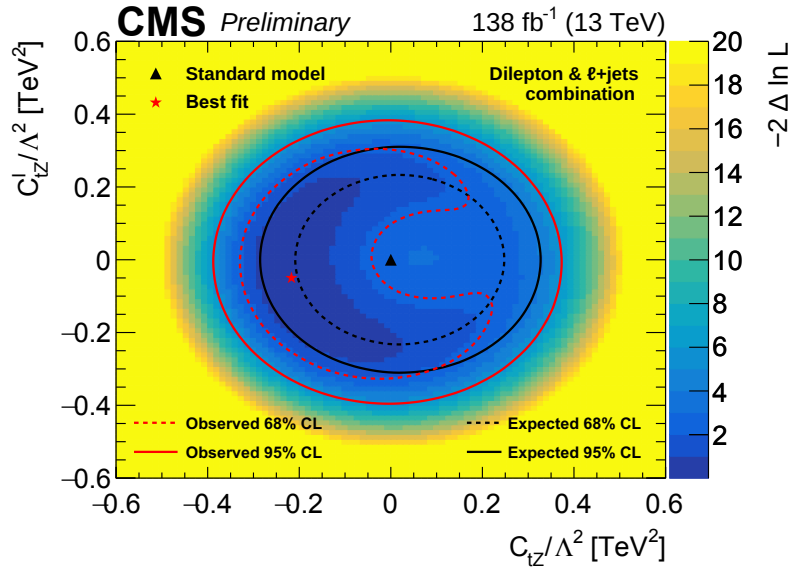
the individual interpretations, and provide the best limits to date on the Wilson coefficients c_{tZ} and c_{tZ}^I.

9 Summary

A cross section measurement of top quark pair production in association with a photon ($t\bar{t}\gamma$), using $138\,\text{fb}^{-1}$ of proton-proton collision data at $\sqrt{s} = 13\,\text{TeV}$ recorded with the CMS detector at the CERN LHC, has been presented. The analysis is performed in a fiducial phase space defined by the requirement of exactly one isolated photon, exactly two oppositely charged leptons, and at least one b jet at particle level, including the e^+e^-, $e^\pm\mu^\mp$, and $\mu^+\mu^-$ channels of the $t\bar{t}$ decay. The inclusive cross section is extracted with a template fit to the transverse momentum distribution of the reconstructed photon, and is measured to be $\sigma_{\text{fid}}(\text{pp} \to t\bar{t}\gamma) = 174.4 \pm 2.5\,(\text{stat}) \pm 6.1\,(\text{syst})\,\text{fb}$, in good agreement with the standard model prediction of $\sigma_{\text{SM}}(\text{pp} \to t\bar{t}\gamma) = 153 \pm 25\,\text{fb}$.

Differential cross sections are measured as functions of various kinematic properties of the photon, leptons, and jet, and unfolded to particle level. The comparison to standard model predictions is performed using different parton shower algorithms. The measurement is also interpreted in terms of the standard model effective field theory. Constraints are derived on the Wilson coefficients c_{tZ} and c_{tZ}^I describing the modifications of the $t\bar{t}Z$ and $t\bar{t}\gamma$ interaction vertices. From a combined interpretation of this measurement and another CMS measurement of $t\bar{t}\gamma$ production using the single-lepton final state and the same data set, the best limits on these Wilson coefficients to date are derived.

References

[1] CDF Collaboration, "Evidence for $t\bar{t}\gamma$ production and measurement of $\sigma_{t\bar{t}\gamma}/\sigma_{t\bar{t}}$", *Phys. Rev. D* **84** (2011) 031104, `doi:10.1103/PhysRevD.84.031104`, `arXiv:1106.3970`.

[2] ATLAS Collaboration, "Observation of top-quark pair production in association with a photon and measurement of the $t\bar{t}\gamma$ production cross section in pp collisions at $\sqrt{s} = 7\,\text{TeV}$ using the ATLAS detector", *Phys. Rev. D* **91** (2015) 072007, `doi:10.1103/PhysRevD.91.072007`, `arXiv:1502.00586`.

[3] ATLAS Collaboration, "Measurement of the $t\bar{t}\gamma$ production cross section in proton-proton collisions at $\sqrt{s} = 8\,\text{TeV}$ with the ATLAS detector", *JHEP* **11** (2017) 086, `doi:10.1007/JHEP11(2017)086`, `arXiv:1706.03046`.

[4] CMS Collaboration, "Measurement of the semileptonic $t\bar{t} + \gamma$ production cross section in pp collisions at $\sqrt{s} = 8\,\text{TeV}$", *JHEP* **10** (2017) 006, `doi:10.1007/JHEP10(2017)006`, `arXiv:1706.08128`.

[5] ATLAS Collaboration, "Measurements of inclusive and differential fiducial cross-sections of $t\bar{t}\gamma$ production in leptonic final states at $\sqrt{s} = 13\,\text{TeV}$ in ATLAS", *Eur. Phys. J. C* **79** (2019) 382, `doi:10.1140/epjc/s10052-019-6849-6`, `arXiv:1812.01697`.

[6] ATLAS Collaboration, "Measurements of inclusive and differential cross-sections of combined $t\bar{t}\gamma$ and $tW\gamma$ production in the $e\mu$ channel at $13\,\text{TeV}$ with the ATLAS detector", *JHEP* **09** (2020) 049, `doi:10.1007/JHEP09(2020)049`, `arXiv:2007.06946`.

[7] CMS Collaboration, "Measurement of the inclusive and differential $t\bar{t}\gamma$ cross sections in the single-lepton channel and EFT interpretation at $\sqrt{s} = 13\,\text{TeV}$", `arXiv:2107.01508`. Submitted to *JHEP*.

[8] J. A. Aguilar-Saavedra et al., "Interpreting top-quark LHC measurements in the standard-model effective field theory", LHC TOP WG note CERN-LPCC-2018-01, 2018. `arXiv:1802.07237`.

[9] P.-F. Duan et al., "QCD corrections to associated production of $t\bar{t}\gamma$ at hadron colliders", *Phys. Rev. D* **80** (2009) 014022, `doi:10.1103/PhysRevD.80.014022`, `arXiv:0907.1324`.

[10] K. Melnikov, M. Schulze, and A. Scharf, "QCD corrections to top quark pair production in association with a photon at hadron colliders", *Phys. Rev. D* **83** (2011) 074013, `doi:10.1103/PhysRevD.83.074013`, `arXiv:1102.1967`.

[11] P.-F. Duan et al., "Next-to-leading order QCD corrections to $t\bar{t}\gamma$ production at the 7 TeV LHC", *Chin. Phys. Lett.* **28** (2011) 111401, `doi:10.1088/0256-307X/28/11/111401`, `arXiv:1110.2315`.

[12] A. Kardos and Z. Trócsányi, "Hadroproduction of $t\bar{t}$ pair in association with an isolated photon at NLO accuracy matched with parton shower", *JHEP* **05** (2015) 090, `doi:10.1007/JHEP05(2015)090`, `arXiv:1406.2324`.

[13] F. Maltoni, D. Pagani, and I. Tsinikos, "Associated production of a top-quark pair with vector bosons at NLO in QCD: impact on $t\bar{t}H$ searches at the LHC", *JHEP* **02** (2016) 113, `doi:10.1007/JHEP02(2016)113`, `arXiv:1507.05640`.

[14] P.-F. Duan et al., "Electroweak corrections to top quark pair production in association with a hard photon at hadron colliders", *Phys. Lett. B* **766** (2017) 102, `doi:10.1016/j.physletb.2016.12.061`, `arXiv:1612.00248`.

[15] G. Bevilacqua et al., "Precise predictions for $t\bar{t}\gamma/t\bar{t}$ cross section ratios at the LHC", *JHEP* **01** (2019) 188, `doi:10.1007/JHEP01(2019)188`, `arXiv:1809.08562`.

[16] G. Bevilacqua et al., "Off-shell vs on-shell modelling of top quarks in photon associated production", *JHEP* **03** (2020) 154, `doi:10.1007/JHEP03(2020)154`, `arXiv:1912.09999`.

[17] U. Baur, A. Juste, L. H. Orr, and D. Rainwater, "Probing electroweak top quark couplings at hadron colliders", *Phys. Rev. D* **71** (2005) 054013, `doi:10.1103/PhysRevD.71.054013`, `arXiv:hep-ph/0412021`.

[18] A. Bouzas and F. Larios, "Electromagnetic dipole moments of the top quark", *Phys. Rev. D* **87** (2013) 074015, `doi:10.1103/PhysRevD.87.074015`, `arXiv:1212.6575`.

[19] M. Schulze and Y. Soreq, "Pinning down electroweak dipole operators of the top quark", *Eur. Phys. J. C* **76** (2016) 466, `doi:10.1140/epjc/s10052-016-4263-x`, `arXiv:1603.08911`.

[20] W. Buchmüller and D. Wyler, "Effective lagrangian analysis of new interactions and flavour conservation", *Nucl. Phys. B* **268** (1986) 621, `doi:10.1016/0550-3213(86)90262-2`.

[21] B. Grzadkowski, M. Iskrzyński, M. Misiak, and J. Rosiek, "Dimension-six terms in the standard model Lagrangian", *JHEP* **10** (2010) 085, `doi:10.1007/JHEP10(2010)085`, `arXiv:1008.4884`.

[22] O. Bessidskaia Bylund et al., "Probing top quark neutral couplings in the standard model effective field theory at NLO in QCD", *JHEP* **05** (2016) 052, `doi:10.1007/JHEP05(2016)052`, `arXiv:1601.08193`.

[23] J. A. Aguilar-Saavedra, E. Álvarez, A. Juste, and F. Rubbo, "Shedding light on the $t\bar{t}$ asymmetry: the photon handle", *JHEP* **04** (2014) 188, `doi:10.1007/JHEP04(2014)188`, `arXiv:1402.3598`.

[24] J. Bergner and M. Schulze, "The top quark charge asymmetry in $t\bar{t}\gamma$ production at the LHC", *Eur. Phys. J. C* **79** (2019) 189, `doi:10.1140/epjc/s10052-019-6707-6`, `arXiv:1812.10535`.

[25] J. Alwall et al., "The automated computation of tree-level and next-to-leading order differential cross sections, and their matching to parton shower simulations", *JHEP* **07** (2014) 079, `doi:10.1007/JHEP07(2014)079`, `arXiv:1405.0301`.

[26] P. Nason, "A new method for combining NLO QCD with shower Monte Carlo algorithms", *JHEP* **11** (2004) 040, `doi:10.1088/1126-6708/2004/11/040`, `arXiv:hep-ph/0409146`.

[27] S. Frixione, P. Nason, and C. Oleari, "Matching NLO QCD computations with parton shower simulations: the POWHEG method", *JHEP* **11** (2007) 070, `doi:10.1088/1126-6708/2007/11/070`, `arXiv:0709.2092`.

[28] S. Alioli, P. Nason, C. Oleari, and E. Re, "A general framework for implementing NLO calculations in shower Monte Carlo programs: the POWHEG BOX", *JHEP* **06** (2010) 043, `doi:10.1007/JHEP06(2010)043`, `arXiv:1002.2581`.

[29] J. M. Campbell, R. K. Ellis, P. Nason, and E. Re, "Top-pair production and decay at NLO matched with parton showers", *JHEP* **04** (2015) 114, `doi:10.1007/JHEP04(2015)114`, `arXiv:1412.1828`.

[30] S. Alioli, P. Nason, C. Oleari, and E. Re, "NLO single-top production matched with shower in POWHEG: *s*- and *t*-channel contributions", *JHEP* **09** (2009) 111, `doi:10.1088/1126-6708/2009/09/111`, `arXiv:0907.4076`. [Erratum: `doi:10.1007/JHEP02(2010)011`].

[31] S. Frixione, G. Ridolfi, and P. Nason, "A positive-weight next-to-leading-order Monte Carlo for heavy flavour hadroproduction", *JHEP* **09** (2007) 126, `doi:10.1088/1126-6708/2007/09/126`, `arXiv:0707.3088`.

[32] J. M. Campbell and R. K. Ellis, "MCFM for the Tevatron and the LHC", *Nucl. Phys. B Proc. Suppl.* **205-206** (2010) 10, `doi:10.1016/j.nuclphysbps.2010.08.011`, `arXiv:1007.3492`.

[33] J. M. Campbell, R. K. Ellis, and C. Williams, "Bounding the Higgs width at the LHC using full analytic results for gg $\rightarrow$ e$^-$e$^+\mu^-\mu^+$", *JHEP* **04** (2014) 060, `doi:10.1007/JHEP04(2014)060`, `arXiv:1311.3589`.

[34] NNPDF Collaboration, "Parton distributions for the LHC Run II", *JHEP* **04** (2015) 040, `doi:10.1007/JHEP04(2015)040`, `arXiv:1410.8849`.

[35] NNPDF Collaboration, "Parton distributions from high-precision collider data", *Eur. Phys. J. C* **77** (2017) 663, `doi:10.1140/epjc/s10052-017-5199-5`, `arXiv:1706.00428`.

[36] T. Sjöstrand, S. Mrenna, and P. Z. Skands, "A brief introduction to PYTHIA 8.1", *Comput. Phys. Commun.* **178** (2008) 852, `doi:10.1016/j.cpc.2008.01.036`, `arXiv:0710.3820`.

[37] T. Sjöstrand et al., "An introduction to PYTHIA 8.2", *Comput. Phys. Commun.* **191** (2015) 159, `doi:10.1016/j.cpc.2015.01.024`, `arXiv:1410.3012`.

[38] CMS Collaboration, "Extraction and validation of a new set of CMS PYTHIA8 tunes from underlying-event measurements", *Eur. Phys. J. C* **80** (2020) 4, `doi:10.1140/epjc/s10052-019-7499-4`, `arXiv:1903.12179`.

[39] P. Skands, S. Carrazza, and J. Rojo, "Tuning PYTHIA 8.1: the Monash 2013 tune", *Eur. Phys. J. C* **74** (2014) 3024, `doi:10.1140/epjc/s10052-014-3024-y`, `arXiv:1404.5630`.

[40] CMS Collaboration, "Event generator tunes obtained from underlying event and multiparton scattering measurements", *Eur. Phys. J. C* **76** (2016) 155, `doi:10.1140/epjc/s10052-016-3988-x`, `arXiv:1512.00815`.

[41] CMS Collaboration, "Investigations of the impact of the parton shower tuning in Pythia 8 in the modelling of $t\bar{t}$ at $\sqrt{s} = 8$ and $13\,\text{TeV}$", CMS Physics Analysis Summary CMS-PAS-TOP-16-021, 2016.

[42] J. Alwall et al., "Comparative study of various algorithms for the merging of parton showers and matrix elements in hadronic collisions", *Eur. Phys. J. C* **53** (2008) 473, `doi:10.1140/epjc/s10052-007-0490-5`, `arXiv:0706.2569`.

[43] R. Frederix and S. Frixione, "Merging meets matching in MC@NLO", *JHEP* **12** (2012) 061, `doi:10.1007/JHEP12(2012)061`, `arXiv:1209.6215`.

[44] Y. Li and F. Petriello, "Combining QCD and electroweak corrections to dilepton production in FEWZ", *Phys. Rev. D* **86** (2012) 094034, `doi:10.1103/PhysRevD.86.094034`, `arXiv:1208.5967`.

[45] M. Czakon and A. Mitov, "Top++: A program for the calculation of the top-pair cross-section at hadron colliders", *Comput. Phys. Commun.* **185** (2014) 2930, `doi:10.1016/j.cpc.2014.06.021`, `arXiv:1112.5675`.

[46] M. Aliev et al., "HATHOR: Hadronic top and heavy quarks cross section calculator", *Comput. Phys. Commun.* **182** (2011) 1034, `doi:10.1016/j.cpc.2010.12.040`, `arXiv:1007.1327`.

[47] P. Kant et al., "HATHOR for single top-quark production: Updated predictions and uncertainty estimates for single top-quark production in hadronic collisions", *Comput. Phys. Commun.* **191** (2015) 74, `doi:10.1016/j.cpc.2015.02.001`, `arXiv:1406.4403`.

[48] N. Kidonakis, "Theoretical results for electroweak boson and single-top production", in *XXIII International Workshop on Deep-Inelastic Scattering (DIS2015)*. 2015. `arXiv:1506.04072`. [PoS (DIS2015) 170]. `doi:10.22323/1.247.0170`.

[49] M. Cacciari, G. P. Salam, and G. Soyez, "The anti-k_T jet clustering algorithm", *JHEP* **04** (2008) 063, `doi:10.1088/1126-6708/2008/04/063`, `arXiv:0802.1189`.

[50] M. Cacciari, G. P. Salam, and G. Soyez, "The catchment area of jets", *JHEP* **04** (2008) 005, `doi:10.1088/1126-6708/2008/04/005`, `arXiv:0802.1188`.

[51] GEANT4 Collaboration, "GEANT4—a simulation toolkit", *Nucl. Instrum. Meth. A* **506** (2003) 250, `doi:10.1016/S0168-9002(03)01368-8`.

[52] CMS Collaboration, "Particle-flow reconstruction and global event description with the CMS detector", *JINST* **12** (2017) P10003, `doi:10.1088/1748-0221/12/10/P10003`, `arXiv:1706.04965`.

[53] M. Cacciari, G. P. Salam, and G. Soyez, "FastJet user manual", *Eur. Phys. J. C* **72** (2012) 1896, `doi:10.1140/epjc/s10052-012-1896-2`, `arXiv:1111.6097`.

[54] CMS Collaboration, "Electron and photon reconstruction and identification with the CMS experiment at the CERN LHC", *JINST* **16** (2021) P05014, `doi:10.1088/1748-0221/16/05/P05014`, `arXiv:2012.06888`.

[55] CMS Collaboration, "Performance of the CMS muon detector and muon reconstruction with proton-proton collisions at $\sqrt{s} = 13\,\mathrm{TeV}$", *JINST* **13** (2018) P06015, `doi:10.1088/1748-0221/13/06/P06015`, `arXiv:1804.04528`.

[56] CMS Collaboration, "Inclusive and differential cross section measurements of single top quark production in association with a Z boson in proton-proton collisions at $\sqrt{s} = 13\,\mathrm{TeV}$", CMS Physics Analysis Summary CMS-PAS-TOP-20-010, 2021.

[57] A. Hoecker et al., "TMVA - Toolkit for multivariate data analysis", 2007. `arXiv:physics/0703039`.

[58] CMS Collaboration, "Jet energy scale and resolution in the CMS experiment in pp collisions at 8 TeV", *JINST* **12** (2017) P02014, `doi:10.1088/1748-0221/12/02/P02014`, `arXiv:1607.03663`.

[59] CMS Collaboration, "Identification of heavy-flavour jets with the CMS detector in pp collisions at 13 TeV", *JINST* **13** (2018) P05011, `doi:10.1088/1748-0221/13/05/P05011`, `arXiv:1712.07158`.

[60] Particle Data Group, P. A. Zyla et al., "Review of particle physics", *Prog. Theor. Exp. Phys.* **2020** (2020) 083C01, `doi:10.1093/ptep/ptaa104`.

[61] CMS Collaboration, "Search for WWγ and WZγ production and constraints on anomalous quartic gauge couplings in pp collisions at $\sqrt{s} = 8\,\mathrm{TeV}$", *Phys. Rev. D* **90** (2014) 032008, `doi:10.1103/PhysRevD.90.032008`, `arXiv:1404.4619`.

[62] ATLAS Collaboration, "Measurements of Zγ and Z$\gamma\gamma$ production in pp collisions at $\sqrt{s} = 8\,\mathrm{TeV}$ with the ATLAS detector", *Phys. Rev. D* **93** (2016) 112002, `doi:10.1103/PhysRevD.93.112002`, `arXiv:1604.05232`.

[63] CMS Collaboration, "Measurement of the production cross section for single top quarks in association with W bosons in proton-proton collisions at $\sqrt{s} = 13\,\mathrm{TeV}$", *JHEP* **10** (2018) 117, `doi:10.1007/JHEP10(2018)117`, `arXiv:1805.07399`.

[64] CMS Collaboration, "Precision luminosity measurement in proton-proton collisions at $\sqrt{s} = 13$ TeV in 2015 and 2016 at CMS", *Eur. Phys. J. C* **81** (2021) 800, `doi:10.1140/epjc/s10052-021-09538-2`, `arXiv:2104.01927`.

[65] CMS Collaboration, "CMS luminosity measurement for the 2017 data-taking period at $\sqrt{s} = 13$ TeV", CMS Physics Analysis Summary CMS-PAS-LUM-17-004, 2018.

[66] CMS Collaboration, "CMS luminosity measurement for the 2018 data-taking period at $\sqrt{s} = 13$ TeV", CMS Physics Analysis Summary CMS-PAS-LUM-18-002, 2019.

[67] CMS Collaboration, "Measurement of the inelastic proton-proton cross section at $\sqrt{s} = 13$ TeV", *JHEP* **07** (2018) 161, `doi:10.1007/JHEP07(2018)161`, `arXiv:1802.02613`.

[68] ATLAS Collaboration, "Measurement of the inelastic proton-proton cross section at $\sqrt{s} = 13$ TeV with the ATLAS detector at the LHC", *Phys. Rev. Lett.* **117** (2016) 182002, `doi:10.1103/PhysRevLett.117.182002`, `arXiv:1606.02625`.

[69] S. Argyropoulos and T. Sjöstrand, "Effects of color reconnection on $t\bar{t}$ final states at the LHC", *JHEP* **11** (2014) 043, `doi:10.1007/JHEP11(2014)043`, `arXiv:1407.6653`.

[70] J. Christiansen and P. Skands, "String formation beyond leading colour", *JHEP* **08** (2015) 003, `doi:10.1007/JHEP08(2015)003`, `arXiv:1505.01681`.

[71] M. Bowler, "e^+e^- production of heavy quarks in the string model", *Z. Phys. C* **11** (1981) 169, `doi:10.1007/BF01574001`.

[72] ATLAS Collaboration, CMS Collaboration, and LHC Higgs Combination Group, "Procedure for the LHC Higgs boson search combination in Summer 2011", Technical Report CMS-NOTE-2011-005, ATL-PHYS-PUB-2011-011, 2011.

[73] G. Cowan, K. Cranmer, E. Gross, and O. Vitells, "Asymptotic formulae for likelihood-based tests of new physics", *Eur. Phys. J. C* **71** (2011) 1554, `doi:10.1140/epjc/s10052-011-1554-0`, `arXiv:1007.1727`. [Erratum: `doi:10.1140/epjc/s10052-013-2501-z`].

[74] G. Cowan, "Statistical data analysis". Clarendon Press, Oxford, 1998.

[75] S. Schmitt, "TUnfold, an algorithm for correcting migration effects in high energy physics", *JINST* **7** (2012) T10003, `doi:10.1088/1748-0221/7/10/T10003`, `arXiv:1205.6201`.

[76] J. Bellm et al., "HERWIG 7.0/HERWIG++ 3.0 release note", *Eur. Phys. J. C* **76** (2016) 196, `doi:10.1140/epjc/s10052-016-4018-8`, `arXiv:1512.01178`.

[77] CMS Collaboration, "Development and validation of HERWIG 7 tunes from CMS underlying-event measurements", *Eur. Phys. J. C* **81** (2021) 312, `doi:10.1140/epjc/s10052-021-08949-5`, `arXiv:2011.03422`.

[78] J. A. Aguilar-Saavedra, "A minimal set of top anomalous couplings", *Nucl. Phys. B* **812** (2009) 181, `doi:10.1016/j.nuclphysb.2008.12.012`, `arXiv:0811.3842`.

[79] C. Zhang and S. Willenbrock, "Effective-field-theory approach to top-quark production and decay", *Phys. Rev. D* **83** (2011) 034006, `doi:10.1103/PhysRevD.83.034006`, `arXiv:1008.3869`.

[80] CMS Collaboration, "Measurements of $t\bar{t}$ differential cross sections in proton-proton collisions at $\sqrt{s} = 13$ TeV using events containing two leptons", *JHEP* **02** (2019) 149, `doi:10.1007/JHEP02(2019)149`, `arXiv:1811.06625`.

[81] CMS Collaboration, "Measurement of the top quark polarization and $t\bar{t}$ spin correlations using dilepton final states in proton-proton collisions at $\sqrt{s} = 13$ TeV", *Phys. Rev. D* **100** (2019) 072002, `doi:10.1103/PhysRevD.100.072002`, `arXiv:1907.03729`.

[82] ATLAS and CMS Collaborations, "Combination of the W boson polarization measurements in top quark decays using ATLAS and CMS data at $\sqrt{s} = 8$ TeV", *JHEP* **08** (2020) 051, `doi:10.1007/JHEP08(2020)051`, `arXiv:2005.03799`.